

1 **Merging TEMPEST Microwave and GOES-16 Geostationary IR soundings for**  
2 **improved water vapor profiles**

3  
4 Chia-Pang Kuo<sup>1</sup>, Christian Kummerow<sup>1</sup>

5 <sup>1</sup>Department of Atmospheric Science, Colorado State University, Fort Collins, CO 80523, USA

6  
7 Correspondence to: Chia-Pang Kuo (chia-pang.kuo@colostate.edu)

8  
9 **Abstract.** The Temporal Experiment for Storms and Tropical Systems Demonstration (TEMPEST-D)  
10 demonstrated the capability of CubeSat satellites to provide high-quality, stable microwave signals for  
11 estimating water vapor, clouds, and precipitation from space. Unlike the operational NOAA and MetOp  
12 series satellites, which combine microwave and hyperspectral infrared sensors on the same platforms  
13 to optimize retrievals, CubeSat radiometers such as TEMPEST do not carry additional sensors. In such  
14 cases, the high temporal and spatial resolution and multi-channel measurements from the Advanced  
15 Baseline Imager (ABI) on the next-generation series of Geostationary Operational Environmental  
16 Satellites (GOES-R) are ideal for assisting these smaller, stand-alone radiometers. Based on sensitivity  
17 tests, the water vapor retrievals from TEMPEST are improved by adding water-vapor-sounding,  
18 window and CO<sub>2</sub> channels at 6.2, 6.9, 7.3, 8.4, 10.3, 11.2, 12.3 and 13.3 μm from ABI, which help to  
19 increase the vertical resolution of soundings and reduce retrieval errors. Adding three ABI water-vapor-  
20 sounding channels, under clear sky conditions, retrieval biases and root-mean-square errors improve  
21 by approximately 10 %, while under cloudy skies, biases remain unchanged, but root-mean-square  
22 errors still decrease by 5 %; meanwhile, retrieval biases and root-mean-square errors are substantially  
23 reduced by adding more information from eight ABI bands in both clear and cloudy skies. Humidity  
24 soundings are also validated using coastal radiosonde data from the Integrated Global Radiosonde  
25 Archive (IGRA) from 2019 to 2020. When ABI indicates clear skies, water vapor retrievals improve  
26 somewhat by decreasing the overall bias in the microwave only estimate by roughly 10 %, although  
27 layer root-mean-square errors remain roughly unchanged at 1 g/kg when three or eight ABI channels  
28 are added. When ABI indicates cloudy conditions, there is little change in the results. The small number  
29 of matched radiosondes may limit the observed improvement.

30  
31 **1. Introduction**

32  
33 The Temporal Experiment for Storms and Tropical Systems Demonstration (TEMPEST-D; Reising et al.,  
34 2018) mission was designed to demonstrate the capability of a small radiometer on board a 6U  
35 CubeSat satellite for deriving clouds, water vapor, and precipitation. The CubeSat, including the flight  
36 system and the TEMPEST-D radiometer, is 10 cm x 20 cm x 34 cm and weighs 11.2 kg. Although the size  
37 of the TEMPEST-D is much smaller than instruments such as the operational Microwave Humidity  
38 Sounders (MHS on NOAA-18/19 and MetOp-A/B/C), which weigh about 63 kg, the TEMPEST-D  
39 radiometer demonstrated the capability to provide comparable well-calibrated microwave (MW)  
40 measurements (Berg et al., 2021; Brown et al., 2023). In addition, Schulte et al. (2020) introduced the  
41 bias correction of Earth incidence angle (EIA) (Schulte and Kummerow, 2019) in the Optimal Estimation  
42 (OE; Rodgers, 2000) framework with TEMPEST-D and demonstrated the potential of getting consistent  
43 retrievals from a fleet of TEMPEST sensors observing the same spot with different EIAs. Radhakrishnan

Deleted: and

Deleted: mm

Deleted: Under

Deleted: %.

48 et al. (2022) estimated surface rainfall by machine-learning methods and showed that retrieved rainfall  
49 using TEMPEST-D channels was consistent with the multi-radar/multi-sensor system (MRMS) rainfall  
50 products over the Continental United States. The success of TEMPEST-D led to flying a second TEMPEST  
51 unit in conjunction with the Compact Ocean Wind Vector Radiometer (COWVR;  
52 <https://podaac.jpl.nasa.gov/COWVR-TEMPEST>) currently in orbit aboard the International Space  
53 Station.

54  
55 Several studies have shown the capability of retrieving surface and atmospheric variables over the  
56 ocean under non-raining conditions using Optimal Estimation (OE) techniques. Elsaesser and  
57 Kummerow (2008) retrieved total precipitable water (TPW), surface wind, and cloud liquid water path  
58 (CLWP) using observations from the Advanced Microwave Scanning Radiometer-Earth Observing  
59 System (AMSR-E), the Special Sensor Microwave/Imager (SSM/I), and the Tropical Rainfall Measuring  
60 Mission (TRMM) Microwave Imager (TMI) using the same OE configurations. This was later expanded  
61 to the Global Precipitation Measurement (GPM) Microwave Imager (GMI) (Duncan and Kummerow,  
62 2016). The Colorado State University 1 D variational inversion algorithm (CSU 1DVAR) has been  
63 validated by comparing results with other independent products, showing that CSU 1DVAR can provide  
64 consistent results across a broad spectrum of sensors (Elsaesser and Kummerow, 2008; Duncan and  
65 Kummerow, 2016; Schulte and Kummerow, 2019; Schulte et al., 2020). A conceptually similar OE  
66 method is employed in the Microwave Integrated Retrieval System (MiRS; Boukabara et al., 2011,  
67 2013, 2018) designed to provide various atmospheric and surface parameters (skin temperature,  
68 surface emissivity, and profiles of temperature, water vapor, non-precipitating clouds, and  
69 precipitations) under all sky conditions over ocean and land surfaces. Due to its flexible structure, MiRS  
70 is used operationally at NOAA and supports measurements from multiple MW instruments, including  
71 the TMI, GMI, MHS, Atmospheric Microwave Sounding Unit (AMSU), SSM/I, Special Sensor Microwave  
72 Imager/Sounder (SSMIS), and Advanced Technology Microwave Sounder (ATMS).

73  
74 Infrared (IR) sounders, and especially hyperspectral IR sounders, while limited to clear sky conditions,  
75 have distinct advantages for deriving temperature and moisture profiles due to their sharper weighting  
76 functions, particularly in the upper troposphere when no clouds are present. Using MW measurements  
77 from AMSU-A and MHS plus IR observations from the Infrared Atmospheric Sounding Interferometer  
78 (IASI) on board the MetOp platforms, Aires (2011) and Aires et al. (2011, 2012) significantly reduced  
79 the errors of retrieving temperature and water vapor profiles under clear sky conditions over the  
80 ocean by comparing with retrievals using individual MW or IR instruments alone. Under the European  
81 Space Agency Water Vapour Climate Change Initiative project (Siddans et al., 2015; Siddans, 2019),  
82 Trent et al. (2023) validated 9.5 years of atmospheric profiles retrieved from MetOp MW and IR  
83 observations and showed that global biases of temperature and water vapor are within 0.5 K and 10 %,  
84 respectively, making the retrieval products an important climate data record.

85  
86 In addition to MW and IR measurements on the MetOp platforms, Milstein and Blackwell (2016) also  
87 showed the advantages of using MW and IR spectral bands from the Atmospheric Infrared Sounder  
88 (AIRS) and AMSU on the Aqua satellite as well as from the Cross-Track Infrared Sounder (CrIS) and  
89 ATMS on the Suomi National Polar-orbiting Partnership satellite (Suomi NPP) for temperature and  
90 water vapor retrievals. The NOAA Unique CrIS/ATMS Processing System (NUCAPS; Gambacorta et al.,  
91 2012) was built specifically to retrieve global atmospheric profiles using MW sensors (AMSU, ATMS,

92 and MHS) and hyperspectral IR instruments (AIRS, CrIS, or IASI) under non-precipitating conditions with  
93 up to 80 % effective cloud fraction. Sun et al. (2017) used radiosonde data to assess the sounding  
94 products from NUCAPS, indicating small biases in the lower atmosphere for temperature profiles of  
95 less than 0.5 K and less than 20 % for water vapor profiles. These profiles have been further improved  
96 by Ma et al. (2021), who applied a neural network technique to enhance the retrieved atmospheric  
97 profiles in NUCAPS products by using IR channels on the next-generation series of Geostationary  
98 Operational Environmental Satellites (GOES-R; Schmit et al., 2008). The root-mean-square error of  
99 retrieved temperature and humidity profiles in that study decreased by more than 30 % from the  
100 surface up to 700 hPa. Thus, while it seems clear from these previous studies that merging IR and MW  
101 soundings from the same platforms is beneficial, CubeSat sounders such as TEMPEST or the Time-  
102 Resolved Observations of Precipitation structure and storm Intensity with a Constellation of Smallsats  
103 (TROPICS; Blackwell et al., 2018) do not generally fly in tandem with hyperspectral IR sounders. In this  
104 case, it is useful to examine if there are benefits to merging the stand-alone passive MW sensors with  
105 geostationary IR sounding channels.

Deleted: -

106 The Advanced Baseline Imager (ABI), on board the GOES-R satellite series, observes the full disk of the  
107 Earth every 10 minutes (15 minutes prior to April 2019), measuring in the visible (VIS), near-IR, and IR  
108 spectral bands with spatial resolutions from 0.5 to 2 km. Except for the ozone absorption band at 9.6  
109  $\mu\text{m}$  (ABI channel 12), ABI channels 8 to 16 (6.2 to 13.3  $\mu\text{m}$ ) have different degree of humidity  
110 sensitivities and are suitable for deriving water vapor profiles with similar vertical resolution to the  
111 operational MW sensors (Schmit et al., 2008; Goodman et al., 2019; Li et al., 2019). Due to the high  
112 spatial and temporal resolutions from GOES-R ABI observations over large regions, the ABI sensor can  
113 always be matched with stand-alone MW radiometers over the sensed hemisphere, as illustrated by  
114 Ma et al. (2021). This study thus focuses on the enhancement in water vapor retrievals that may be  
115 achieved when ABI IR sounding channels are added to the TEMPEST-D MW channels.

Deleted: Three water vapor channels at (6.2, 6.9, and 7.3 mm) make ABI...

Deleted: water vapor

## 118 2. Data

119  
120 The TEMPEST-D satellite (Reising et al., 2018) was deployed from the International Space Station on  
121 July 13, 2018, into the Low Earth Orbit. The initial orbit height was 400 km with a 51.6° inclination,  
122 observing an 825 km wide swath from the initial height. The mission successfully demonstrated both  
123 the maneuverability of CubeSats to fly in closely maintained formations as well as the calibration  
124 stability of the MW radiometer (Berg et al., 2021). The TEMPEST-D passive MW radiometer scanned  
125 Earth in a cross-track mode and measured five channels at 87, 164, 174, 178, and 181 GHz with quasi-  
126 horizontal polarization, except for 87 GHz, which measured quasi-vertical polarization. The spatial  
127 resolutions of TEMPEST-D at the nadir were 14 km at 164 to 181 GHz and 28 km at 87 GHz. While the  
128 data is not complete due to difficulties with the data receiving station at Wallops Island, Virginia, USA,  
129 all available TEMPEST-D datasets can be requested through the website <https://tempest.colostate.edu>.  
130 TEMPEST-D was deorbited on June 22, 2021. A second copy of TEMPEST was launched on Dec. 21,  
131 2021, and is operating on the International Space Station in conjunction with COWVR. Data is available  
132 from the National Aeronautics and Space Administration (NASA) Physical Oceanography Distributed  
133 Active Archive Center (PODAAC) housed at NASA's Jet Propulsion Laboratory. Because the instruments  
134 and orbits are identical, the results presented here apply to both sensors.

140 The GOES-16 (Schmit et al., 2008; Li et al., 2019) is the first of the GOES-R series satellites and was  
 141 launched on November 19, 2016, carrying several instruments, including ABI. GOES-16 replaces GOES-  
 142 13 and is located at longitude 75.2°W in a geostationary orbit (35786 km altitude), observing from  
 143 latitude 81.32°N to 81.32°S and from longitude 156.30°W to 6.30°E. This covers North and South  
 144 America, the eastern Pacific Ocean, and the Atlantic Ocean to the west coast of Africa. The ABI sensor  
 145 measures 16 spectral channels from VIS to IR bands (0.47 to 13.3 μm) with spatial resolutions ranging  
 146 from 0.5 km at 0.64 μm to 2.0 km in the IR. The eight ABI water-vapor-sensitive channels at 6.2, 6.9,  
 147 7.3, 8.4, 10.3, 11.2, 12.3 and 13.3 μm are used to enhance the TEMPEST-D retrieved water vapor  
 148 profiles. While the ABI window and CO<sub>2</sub> channels (8.4, 10.3, 11.2, 12.3 and 13.3 μm) have information  
 149 that is similar with the TEMPEST window channels, more measurements provide more information  
 150 content to help constrain retrievals in a way used in the hyperspectral IR retrievals (Aires 2011; Aires et  
 151 al., 2011, 2012; Gambacorta et al., 2012; Siddans et al., 2015). To ensure spatial and temporal  
 152 consistency between TEMPEST-D and the GOES-16, the nearest geolocated ABI full disk pixels from ABI  
 153 Radiances (RadF), Clear Sky Masks (ACMF), Cloud Top Phase (ACTPF), and Cloud Top Pressure (CTPF)  
 154 products are averaged to match the geolocated TEMPEST-D pixels in space and time. The GOES-16  
 155 products can be downloaded through the Comprehensive Large Array Data Stewardship System  
 156 (CLASS). Although GOES-17 also covers parts of the TEMPEST-D operational period, its products are not  
 157 used to avoid all issues related to the cooling system, as described in [https://www.goes-](https://www.goes-<br/>
  158 r.gov/users/GOES-17-ABI-Performance.html)

- Deleted: Only the three
- Deleted: -sounding
- Deleted: 7
- Deleted: add information, these channels
- Deleted: largely redundant
- Deleted: .
- Deleted: products, all
- Deleted: from ABI,
- Deleted: 28 km
- Deleted: horizontal resolution
- Deleted: appended to TEMPEST-D observation locations and times...

159  
 160 Except for satellite observations and products mentioned above, auxiliary data, including surface wind  
 161 speed and direction, surface pressure, surface skin temperature, and temperature profiles, are also  
 162 used to constrain the retrievals. These are taken from the ERA5 (Hersbach et al., 2020), accessed  
 163 through the website <https://www.ecmwf.int/en/forecasts/dataset/ecmwf-reanalysis-v5>. The hourly  
 164 ERA5 data used in the study are 0.5° x 0.5° with 27 pressure levels from 1000 to 100 hPa. The vertical  
 165 resolution (in pressure coordinates) consists of 25 hPa intervals from 1000 to 750 hPa, 50 hPa intervals  
 166 from 750 to 250 hPa, and 25 hPa intervals from 250 to 100 hPa. One hour temporal resolution and 0.5°  
 167 spatial resolution from ERA5 is used to define unobserved surface conditions as well as the  
 168 temperature profiles. The auxiliary surface parameters and temperature profiles are linearly  
 169 interpolated in space and time to match the TEMPEST-D observations. The interpolated ERA5 auxiliary  
 170 data may not reflect the actual conditions at the satellite overpass location and time, so when  
 171 compared with in situ measurements, retrievals may be degraded by using the non-representative  
 172 auxiliary data.

### 174 3. Methods

176 In satellite remote sensing, OE is a widely utilized technique to retrieve atmospheric components  
 177 (Rodgers, 2000; Elsaesser and Kummerow, 2008; Boukabara et al., 2011; Siddans et al., 2015; Duncan  
 178 and Kummerow, 2016; Schulte and Kummerow, 2019; Schulte et al., 2020). In OE, the state parameters  
 179 and measurement errors are all assumed to follow a Gaussian distribution, and the atmospheric states  
 180 being retrieved,  $x$ , are optimally estimated by minimizing the cost function  $J$ ,

$$181 \quad J = (x - x_a)^T S_a^{-1} (x - x_a) + [y - f(x)]^T S_y^{-1} [y - f(x)], \quad (1)$$



195

196 where  $x_a$  is the a priori information about the state vector  $x$ ,  $y$  is the measurement vector,  $f(x)$  is a  
197 forward model simulating measurements for a given state  $x$ ,  $S_a$  is the covariance matrix of a priori, and  
198  $S_y$  is the covariance matrix of measurement errors (Rodgers, 2000). The minimization of  $J$  is achieved  
199 by iteratively solving for the state vector  $x$  using the Gauss-Newton method. Following Eq. 5.29 in  
200 Rodgers (2000), the convergence criteria are achieved when

201

$$202 \quad d_i^2 = (x_i - x_{i+1})^T S^{-1} (x_i - x_{i+1}) \ll n, \quad (2)$$

203

204 where  $d$  measures the change in the state vector between  $i$ th and  $i+1$  iteration, and  $n$  is the  
205 number of retrieved variables (levels of water vapor and/or layers of clouds in this study). The solution  
206 is said to have converged when the residual is one tenth the number of the retrieved variables in the  
207 study. This is consistent with the definition from Eq. (2) that the error weighted increment is much less  
208 than the number of the retrieved variables. The a priori state vector  $x_a$  is used as the initial guess at  
209 the beginning of the iteration. The a priori information  $x_a$  and its uncertainty  $S_a$  are derived from  
210 monthly ERA5 humidity and cloud profiles over the ocean;  $x_a$  describes the mean state of the profiles,  
211 and  $S_a$  accounts for the variation of the states. If sky conditions are known from GOES-16 cloud masks,  
212  $x_a$  and  $S_a$  obtained from clear or cloudy conditions will be used in the retrievals, or otherwise, a priori  
213 values computed from all-sky conditions will be used.

214

215 The state vector  $x$  comprises the water vapor mixing ratio at different pressure levels and/or clouds.  
216 The number of selected water vapor levels depends on the number of channels and the assumptions of  
217 clouds. The selected water vapor levels are evenly distributed in pressure levels at 1000, 900, 800, 600,  
218 and 400 hPa for TEMPEST only, and 1000, 950, 875, 800, 700, 600, 450, and 350 hPa when both  
219 TEMPEST and ABI channels are used. The remaining water vapor levels are linearly interpolated.  
220 Following previous studies (Schulte and Kummerow, 2019; Schulte et al., 2020), clouds are inserted  
221 into single layers containing liquid and/or ice clouds in the profiles. Since passive MW sensors do not  
222 have information about cloud top height, if clouds are assumed to be present, the state vector will  
223 contain one layer of liquid and one layer of ice clouds with liquid cloud top at 900 hPa and ice cloud top  
224 at 300 hPa. If cloud information is available from GOES-16 products, liquid clouds and/or ice clouds can  
225 also be inserted following GOES-16 cloud information as listed in Table 1. The table allows for  
226 experiments where the GOES-16 is used simply to determine if there are clouds in the field of view  
227 (FOV) or the actual cloud properties. If GOES-16 is only used to make the clear or cloudy  
228 determination, then the cloud fraction is set to 0 or 1, respectively. TEMPEST-D, by itself, has no ability  
229 to retrieve the cloud fraction. If details of the cloud field are used, the cloud fraction is set accordingly.

230

231

232

233 Table 1. The retrieval configurations under clear and cloudy conditions with and without GOES-16  
234 cloud information. [ABI means using eight ABI channels 8, 9, 10, 11, 13, 14, 15 and 16 \(6.2, 6.9, 7.3, 8.4,](#)  
235 [10.3, 11.2, 12.3 and 13.3  \$\mu\text{m}\$ \).](#) [ABI 3W means using three ABI water-vapor-sounding channels 8, 9 and](#)  
236 [10 \(6.2, 6.9 and 7.3  \$\mu\text{m}\$ \).](#) CF, CH, and CP represent cloud fraction, cloud height, and cloud phase,  
237 respectively.

238

Sensors	Using GOES-16 cloud products	
	Clear sky	Cloudy sky
TEMPEST+ABI ( <u>13 channels</u> ) or TEMPEST+ABI <u>3W</u> (8 channels) or TEMPEST (5 channels)	1. No, set CF to 1 2. Yes, set CF to 0	1. No, set CF to 1 2. Yes, set CF from GOES-16 3. Yes, set CF, CH, and CP from GOES-16

Formatted Table

239

240

241

242

243

244

245

246

247

248

249

250

251

252

253

254

255

256

257

258

259

260

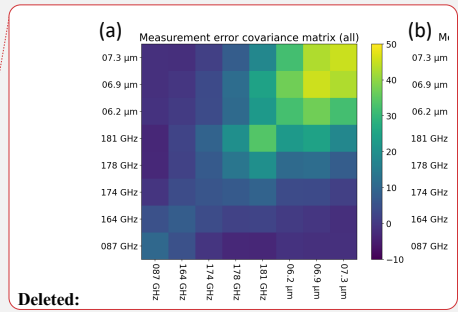
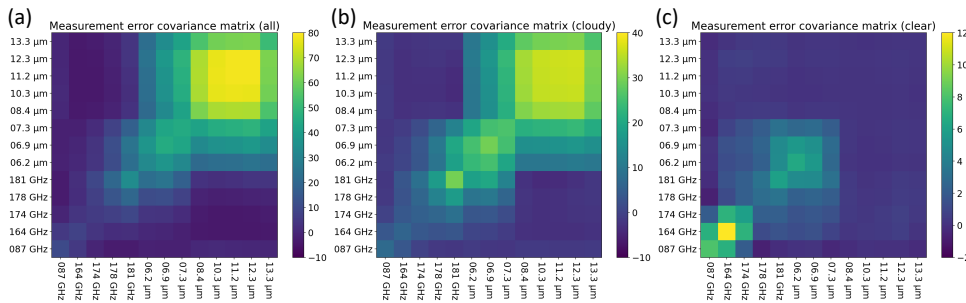
261

262

263

The measurement error covariance matrix  $S_y$  is derived from two uncertainty sources: the radiometer and the forward model (Elsaesser and Kummerow, 2008; Duncan and Kummerow, 2016; Schulte and Kummerow, 2019; Schulte et al., 2020). The noise equivalent differential temperature (NEDT) values are represented as the radiometer measurement errors for each sensor channel. For TEMPEST from 87 to 181 GHz, the NEDT values are 0.20, 0.35, 0.55, 0.55, and 0.75 K, respectively, which are evaluated between 275 and 315 K (Berg et al., 2021; Padmanabhan et al., 2021). The NEDT values of ABI are 0.1 K for all ABI IR channels, except for band 16, which is 0.3 K, and are evaluated at 300 K (Goodman et al., 2019; GOES-R Series, 2022). The forward model uncertainties are approximated by comparing simulated satellite observations using full ERA5 profiles to degraded simulated measurements using the assumptions made in the OE retrievals, as described above. While the radiative transfer model is assumed to contain no errors, errors are introduced when complex water vapor profiles are replaced by simplified water vapor profiles at the [previous](#) prescribed [retrieval](#) levels, and complex cloud vertical profiles are replaced by single liquid and ice cloud layers containing the equivalent cloud water path. The measurement error covariance matrix  $S_y$  is then derived from the NEDT values and the estimated forward model errors. Figures 1(a), 1(b), and 1(c) show the  $S_y$  estimated from all, cloudy and clear skies, respectively, based on oceanic ERA5 profiles. Since ERA5 profiles most often contain some degree of clouds, Figs. 1(a) and 1(b) have similar patterns, and channels having similar water vapor sensitivity are more correlated with each other. On the other hand, due to much lower atmospheric absorption in the clear skies, the surface-sensitive TEMPEST channels (87 and 164 GHz) have higher correlations among themselves as in Fig. 1(c), although with smaller overall  $S_y$  values than in Figs. 1(a) and 1(b).

264



Deleted:

266 Figure 1. Measurement error covariance matrix  $S_y$ , for five TEMPEST-D MW and eight ABI IR channels  
267 derived from ERA5 profiles under (a) all sky, (b) cloudy sky, and (c) clear sky conditions over the ocean.  
268 The unit of the color is  $K^2$ .

Deleted: three

270  
271 The forward model is composed of two radiative transfer models: one simulates MW observations, and  
272 the other computes IR measurements. In the study, the Community Radiative Transfer Model (CRTM;  
273 Liu et al., 2012; Johnson et al., 2023) version 2.3.0 is used to calculate the observed brightness  
274 temperature for the ABI IR channels. The model can be downloaded through the website  
275 <https://github.com/JCSDA/crtm>. To simulate TEMPEST MW observations, an Eddington approximation,  
276 as described in Schulte and Kummerow (2019) and Schulte et al. (2020), is used. The Monochromatic  
277 Radiative Transfer Model (MonoRTM; <https://github.com/AER-RC/monoRTM>; Clough et al., 2005) is  
278 used to generate the atmospheric absorption while the ocean surface MW emissivity is computed  
279 using the FAST microwave Emissivity Model version 6 (FASTEM-6; Kazumori and English, 2015).

Deleted: Clouds

280  
281 In the forward model, clouds are assumed to be homogeneously distributed in single layers. The cloud  
282 top pressure is 900 hPa for liquid clouds and 300 hPa for ice clouds if no cloud top heights are assigned  
283 from GOES-16 products, as described earlier. The CRTM default liquid and ice cloud optical properties  
284 are used to simulate IR brightness temperature with 12 and 30  $\mu\text{m}$  effective radius for liquid and ice  
285 clouds, respectively. The MW optical properties of liquid clouds are generated by Lorenz-Mie theory  
286 (van de Hulst, 1957; Bohren and Huffman, 1998), assuming the droplet is spherical with a radius of 12  
287  $\mu\text{m}$  and is monodisperse in particle size distribution (PSD). The radiative properties of ice clouds in the  
288 MW spectrum are computed using the single-scattering property databases for non-spherical ice  
289 particles from Liu (2008) and Nowell et al. (2013) following the analysis of Schulte and Kummerow  
290 (2019). The databases are derived by the discrete-dipole approximation method (Draine and Flatau,  
291 1994). The microphysical properties of ice clouds used to derive the scattering properties are assumed  
292 to have the PSD from Field et al. (2007) with a constant density of  $100 \text{ g/cm}^3$  and have ice habits: 6  
293 bullet rosettes (crystal size  $< 800 \mu\text{m}$ ) and aggregates of 400  $\mu\text{m}$  rosettes (crystal size  $\geq 800 \mu\text{m}$ ). The  
294 spectral inconsistency of cloud optical properties and miss-representing ice clouds can be two of the  
295 major error sources in radiative transfer simulations (Kulie et al., 2010; [Yang et al., 2018](#); Ringerud et  
296 al., 2019; Schulte and Kummerow, 2019; [Yi et al., 2020](#)), but are not considered here.

Deleted: Ice

Deleted: one

297  
298 The monthly means and variability of water vapor mixing ratios from ERA5 above 200 hPa are  
299 extremely small, as shown in Fig. 2. The sensor responses to these small amounts of stratospheric  
300 water vapor are less than the noise of 0.2 to 0.75 K for TEMPEST and 0.1 to 0.3 K for ABI. Therefore,  
301 the water vapor mixing ratio was set to the monthly mean climatology above 200 hPa and is not  
302 retrieved explicitly with the available channels.

303  
304

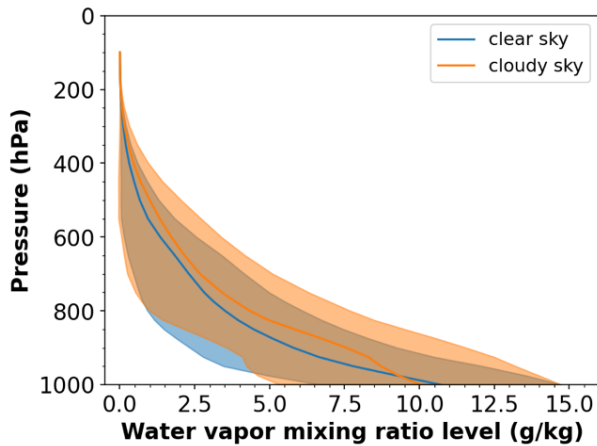


Figure 2. Monthly mean and standard deviation ( $\sigma$ ) of water vapor profiles under clear and cloudy conditions over the ocean between  $\pm 60^\circ$  latitudes from ERA5 in May 2020. Blue color represents water vapor in clear skies, while orange color shows water vapor in cloudy skies. Solid lines are mean water vapor profiles, and shaded areas are standard deviations.

With the model configuration described above and a priori atmospheric temperature and water vapor profiles from ERA5 shown in Figs. 3(a) and 3(b), the sensitivity of water vapor to five TEMPEST-D MW channels and eight ABI IR bands is represented by the clear sky Jacobians shown in Fig. 3(c), and in the cloudy sky Fig. 3(d) presents the Jacobians of water vapor and clouds. For humidity, all TEMPEST MW and ABI IR channels have different degrees of sensitivity along the altitude axis. In clear or cloudy skies, three ABI water-vapor-sounding channels (6.2 to 7.3  $\mu\text{m}$ ) only provide signals for the upper atmosphere. However, signals of water vapor are sensed from the surface to the top of the atmosphere by the TEMPEST MW bands under both clear and cloudy conditions and by ABI window and  $\text{CO}_2$  bands (8.4 to 13.3  $\mu\text{m}$ ) in the clear sky. Although the water vapor sensitivity is substantially reduced under liquid clouds in ABI window and  $\text{CO}_2$  bands, TEMPEST 87 and 164 GHz window bands have significant sensitivity to water vapor and liquid clouds through the entire lower atmosphere. Except for the TEMPEST 87 GHz band, all remaining TEMPEST channels have sensitivity to ice clouds. Overall, as also shown in the studies mentioned in the introduction (Aires, 2011; Milstein and Blackwell, 2016; Sun et al., 2017; Ma et al., 2021; Trent et al., 2023), Figs. 3(c) and 3(d) demonstrate the advantage of merging IR and MW spectral bands in soundings: MW channels have humidity signals under cloudy conditions, IR water-vapor-sounding bands provide extra information about the upper atmosphere, and IR window and  $\text{CO}_2$  channels have humidity sensitivity in the clear sky.

Deleted: three

Deleted: present

Deleted: under the same conditions,

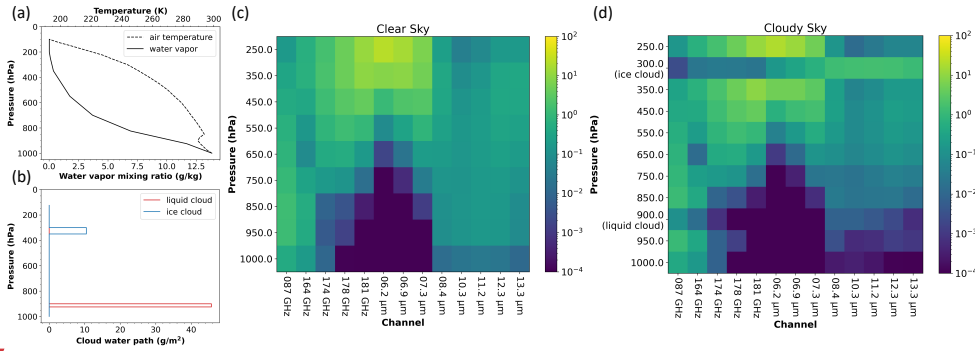
Deleted: by the TEMPEST MW bands

Deleted: .

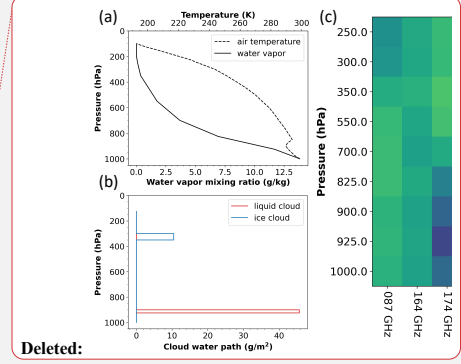
Deleted: spectral

Deleted: spectral

Deleted: and IR



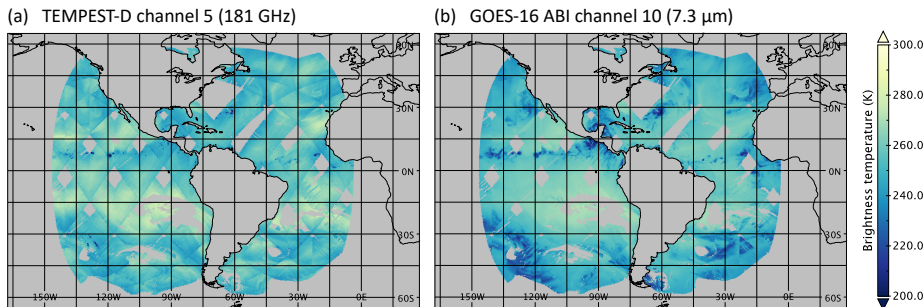
343 Figure 3. An example of water vapor and cloud Jacobians and the ERA5 profiles over the ocean used to  
 344 compute the Jacobians. (a) Profiles of air temperature and water vapor. (b) Liquid and  
 345 cloud layers. (c) Water vapor Jacobians from 250 to 1000 hPa in the clear sky as a function of sensor  
 346 channels (TEMPEST-D from 87 to 181 GHz and ABI from 6.2 to 13.3 μm). (d) The same as (c) but for  
 347 water vapor Jacobians from 250 to 1000 hPa and Jacobians of liquid (cloud top at 900 hPa) and ice  
 348 (cloud top at 300 hPa) clouds in the cloudy sky. The unit of the color for water vapor Jacobians is  
 349 K/g/kg, and for liquid and ice cloud Jacobians is K/g/m<sup>2</sup>.



Deleted: 7

Deleted: 7

351  
 352  
 353 Given the frequent observation from GOES-R ABI, the data can be readily merged with TEMPEST-D.  
 354 Figure 4 shows the overlap of the two sensors over the ocean. Gaps between MW orbits, as well as  
 355 cloudy regions where ABI detects clouds, are evident in both images. Even though ABI cannot be used  
 356 for sounding in cloudy atmospheres, using the ABI cloud products can still provide retrievals some prior  
 357 knowledge about clouds (cloud fraction, phase, and height), which will be shown to positively impact  
 358 the TEMPEST-D MW retrievals. The next section will explore retrieval sensitivities under clear and  
 359 cloudy conditions using synthetic TEMPEST-D and ABI observations simulated from ERA5 profiles.  
 360 Retrieved water vapor profiles are then validated against in situ radiosonde humidity measurements  
 361 under different retrieval assumptions, as listed in Table 1.  
 362  
 363



364

367 Figure 4. Collocated TEMPEST-D and GOES-16 ABI observations over the ocean on 2020/06/01 for (a)  
368 TEMPEST-D channel 5 (181 GHz) and for (b) ABI channel 10 (7.3 μm).

369  
370

## 371 4. Results

372

### 373 4.1. Sensitivity Tests

374

375 Observations for the TEMPEST five (87, 164, 174, 178, and 181 GHz) and ABI eight (6.2, 6.9, 7.3, 8.4,  
376 10.3, 11.2, 12.3, and 13.3 μm) channels are simulated using temperature, humidity, cloud profiles,  
377 surface temperature, and surface wind speed and direction from ERA5 over the ocean with viewing  
378 angles corresponding to TEMPEST and ABI instruments respectively. All data corresponds to May 27,  
379 2020. Since the true states from the ERA5 data are known, the retrieval accuracy can be evaluated  
380 using the computed observed brightness temperature under different scenarios.

381

#### 382 4.1.1. Case studies

383

384 Two cases are used to illustrate the humidity retrievals, first using only the TEMPEST sensor, then  
385 adding three ABI water-vapor-sounding channels, and then using eight ABI bands in clear and cloudy  
386 sky scenes. These are shown in Fig. 5. While the retrieved profiles do not change dramatically, the  
387 additional ABI channels can be seen to improve the mid-tropospheric biases, as shown in Figs. 5(b) and  
388 5(d), especially using eight ABI bands in Fig. 5(b) and adding three ABI water vapor channels in Fig. 5(d).  
389 Although the retrieved water vapor profiles are over- and under-estimated along the height when  
390 compared to the true ERA5 values, Figs. 5(a) and 5(b) reveal that the retrievals using eight extra ABI IR  
391 channels improve significantly with respect to both bias and standard deviation under clear condition  
392 where five ABI window and CO<sub>2</sub> bands provide additional signal from the lower atmosphere in addition  
393 to three ABI water vapor channels giving upper atmosphere information shown in Fig. 3(c). In the  
394 cloudy scene, since ABI window and CO<sub>2</sub> channels are heavily affected by clouds as Fig. 3(d), Figs. 5(c)  
395 and 5(d) show that water vapor retrievals are slightly degraded by using eight ABI channels than by  
396 adding three ABI water vapor bands, which improve retrievals above the 800 hPa level where the ABI  
397 water-vapor-sounding channels are expected to add the most information. While overall biases and  
398 standard deviations also decrease for both examples, it is apparent that ABI has little influence over  
399 the low-level water vapor and that most of the improvement actually comes from the mid to upper  
400 troposphere.

401

402

Deleted: three

Deleted: 7

Deleted: and

Deleted: water-vapor-sounding

Deleted: ) respectively.

Deleted: Fig

Deleted: reveals

Deleted: three

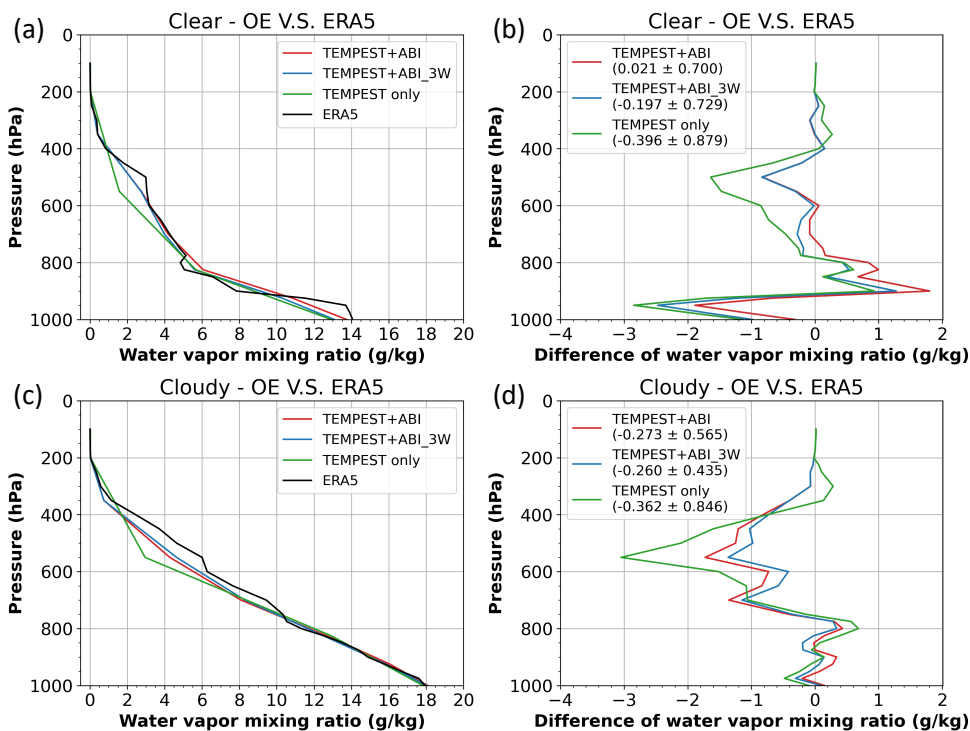
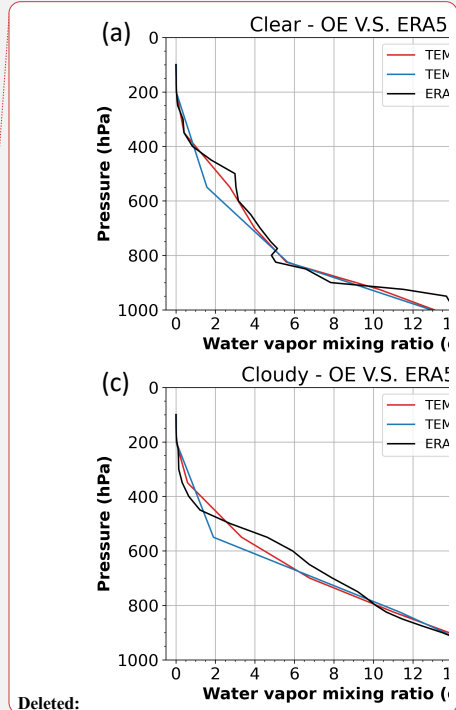


Figure 5. Two selected cases of retrieved water vapor profiles using the synthetic observations from ERA5 over the ocean on 2020/05/27 and using all-sky a priori. Figures (a) and (b) show retrievals under clear conditions, while cloudy retrievals are presented in Figures (c) and (d). Figures (a) and (c) show the retrieved and ERA5 humidity profiles and the corresponding comparisons between retrievals and ERA5 (retrievals minus ERA5) are presented in Figures (b) and (d). The solid black lines are water vapor profiles from ERA5. The solid red lines are water vapor retrievals using five TEMPEST and eight ABI combined channels, and retrievals using TEMPEST and three ABI water vapor bands are the solid blue lines. The solid green lines are retrievals using the TEMPEST sensor. The number in the parentheses is the bias  $\pm$  standard deviation of the whole profile.

#### 4.1.2. Statistics

Comparisons of humidity retrievals using merged five TEMPEST MW bands and three or eight ABI-sounding channels (6.2 to 13.3  $\mu\text{m}$ ) versus using only the TEMPEST sensor are performed for 1000 randomly selected clear or cloudy sky cases. Based on the GOES-16 ABI cloud mask, there are about 1200 clear sky and 8400 cloudy pixels successfully collocated with TEMPEST on May 27, 2020. Randomly selecting 1000 samples from both clear and cloudy pixels allows fair statistical comparisons



Deleted:

Deleted: Selected

Deleted: , 6.9, and 7

Deleted: Since in the observations

Deleted: 2020/05/27, all clear sky pixels

Deleted: samples

Deleted: about

Deleted: cases are

Deleted: according to the GOES-16 cloud mask, randomly

Deleted: pixels over

Deleted: cases are for



between clear and cloudy regions. The statistics are found independent of how the 1000 samples are randomly selected. Results in clear skies are shown in Fig. 6. As with the case studies, adding ABI channels clearly reduces layer biases and random errors in the retrieved water vapor profiles. Errors in the retrieved water vapor above 800 hPa are significantly smaller when using the five MW bands from TEMPEST in combination with the ABI channels. Particularly, among these three retrieval configurations, with the additional information provided by five ABI window and CO<sub>2</sub> channels (8.4 to 13.3 μm), using eight ABI bands in the water vapor retrievals has the least overall biases and standard deviations and improves retrievals around the surface, where the biases are less than 1 g/kg for using eight ABI and five TEMPEST bands in Fig. 6(a) and are about 1.2 to 1.4 g/kg for using five TEMPEST with/without three ABI water vapor channels in Fig. 6(b) and 6(c). While the overall water vapor biases and standard deviations under clear conditions are reduced only slightly from  $(-0.149 \pm 1.127 \text{ g/kg})$  for TEMPEST only to  $(-0.128 \pm 1.022 \text{ g/kg})$  for TEMPEST+ABI 3W, much larger reductions can be seen in the TEMPEST+ABI retrievals  $(-0.014 \pm 0.944 \text{ g/kg})$  and in the layer values shown in Fig. 6 – starting at 900 hPa and extending all the way to 300 hPa.

- Deleted: , which
- Deleted: about the same no matter
- Deleted: we
- Deleted: the 1000 clear or cloudy samples.
- Deleted: three
- Deleted: three ABI channels.

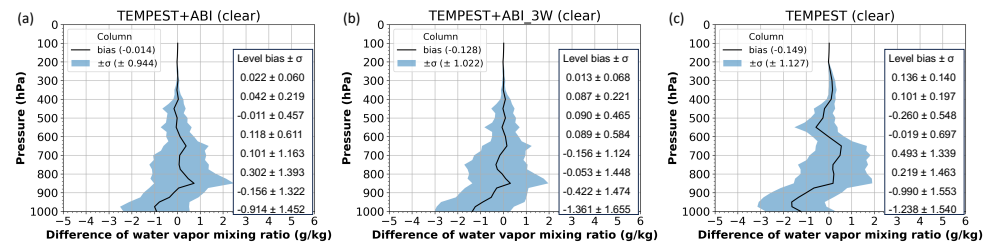
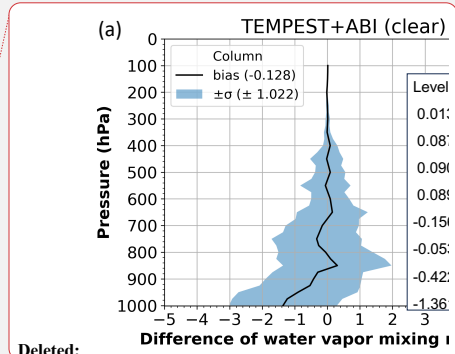


Figure 6. Sensitivity tests of retrieving water vapor profiles using the synthetic measurement from ERA5 under clear conditions over the ocean on 2020/05/27 and using all-sky a priori. Figure (a) shows retrievals using thirteen TEMPEST and ABI combined channels, Figure (b) presents retrievals using five TEMPEST and three ABI water vapor channels, and retrievals using only TEMPEST channels are for Figure (c). Figures (a) to (c) show the difference in water vapor mixing ratio from 1000 randomly selected profiles between retrievals and ERA5 (retrievals minus ERA5) along the height. The solid black lines are the bias value, and the blue shade area is the standard deviation (σ). The included table quantifies the retrieval performance from 300 to 1000 hPa for every 100 hPa.

Similarly, the accuracy of humidity retrievals from 1000 randomly selected cloudy cases using three different sensor configurations is shown in Figs. 7(a) to 7(c). Consistent with the case study and clear sky cases shown in Fig. 6, adding ABI IR channels to the retrievals also reduces biases in the mid-tropospheric layers for cloudy scenes. Due to the lack of sensitivity of ABI channels to the lower atmosphere, as shown in Fig. 3(d), the performance of water vapor retrievals around the surface shows only a negligible improvement in cloudy skies. While the column metrics show unbiased results with or without ABI, the standard deviation of retrieval errors is larger when using TEMPEST-only retrievals (1.022 g/kg) than using merged TEMPEST and three or eight ABI channels (0.949 or 0.898 g/kg). Quantitative comparisons of the vertical profiles in Figs. 7(a) to 7(c) again reveal that the layer biases



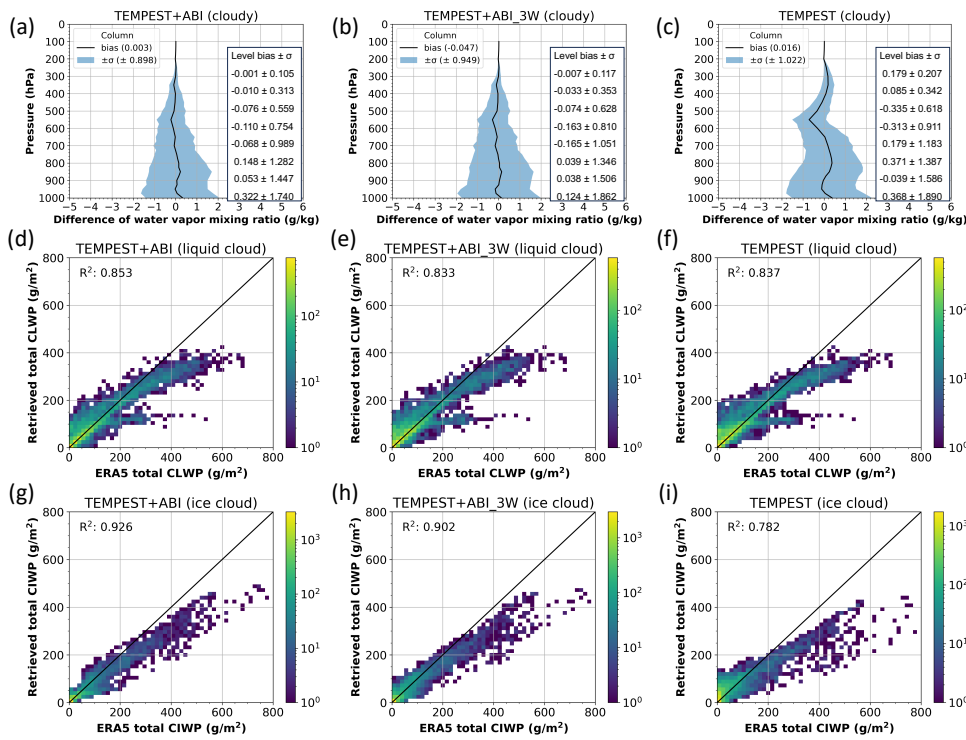
- Deleted:
- Deleted: b
- Deleted: and (b)

- Deleted: two
- Deleted: and
- Deleted: b
- Deleted: three
- Deleted: three
- Deleted: -sounding
- Deleted: Figs. 3(c) and
- Deleted: both clear and
- Deleted: and
- Deleted: b

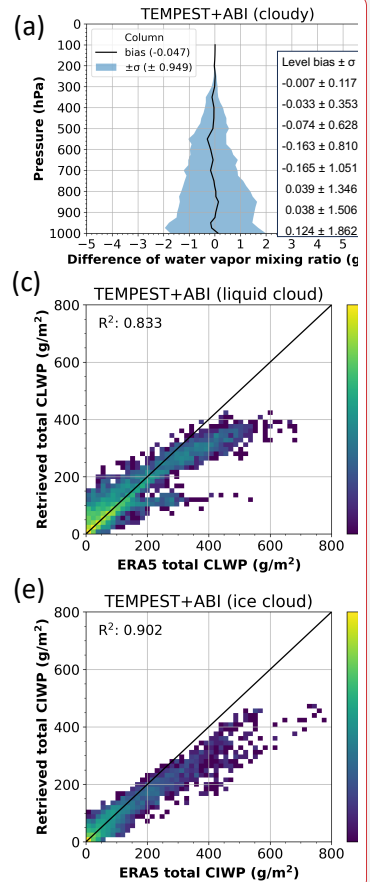
496 are significantly reduced in the TEMPEST+ABI and TEMPEST+ABI 3W retrievals relative to TEMPEST  
 497 alone, reducing the individual layer biases by approximately 50 % (although not uniformly in all layers).  
 498 The overall biases are smaller than in the clear case. The latter is explained by the fact that the all-sky a  
 499 priori guess comes from the climatology of ERA5 profiles for the month, and these profiles  
 500 overwhelmingly contain clouds. The cloudy retrieval is thus less biased in the initial iteration, while the  
 501 clear retrievals must adjust the first guess to correspond to drier conditions when the atmosphere is  
 502 cloud-free. Standard deviations are slightly larger for cloudy scenes, as should be expected from a  
 503 more complex retrieval.

504

505



506 Figure 7. Sensitivity tests of retrievals of water vapor, liquid and ice clouds using synthetic observations  
 507 from ERA5 under cloudy conditions over the ocean on 2020/05/27 and using all-sky a priori. Figures (a),  
 508 (d), and (g) show retrievals using TEMPEST and eight ABI combined channels, Figures (b), (e), and (h)  
 509 present retrievals using merged TEMPEST and three ABI water vapor channels, and retrievals using  
 510 only TEMPEST channels are for Figures (c), (f), and (i). Figures (a) to (c) show the difference in water  
 511 vapor mixing ratio from 1000 randomly selected profiles between retrievals and ERA5 (retrievals minus  
 512 ERA5) along the height. The solid black lines are the bias value, and the blue shade area is the standard  
 513 deviation ( $\sigma$ ). The included table quantifies the retrieval performance from 300 to 1000 hPa for every  
 514



- Deleted:
- Deleted: c
- Deleted: e
- Deleted: b), (d), and
- Deleted: and (b)

100 hPa. Figures (d) to (f) are two-dimensional histograms of retrieved and ERA5 total cloud liquid water path from 8000 randomly selected cases (total number of cloudy pixels is about 8400).  $R^2$  is the coefficient of determination. Color means the number of samples; the solid black lines are the one-to-one lines. Figures (g) to (i) are the same as Figures (d) to (f) but for the total cloud ice water path.

The performance of liquid and ice cloud retrievals is shown in Figs. 7(d) to 7(j). Compared with the cloud liquid water path from ERA5, the liquid cloud retrievals do not improve after incorporating three more ABI water-vapor-sounding channels, shown in Figs. 7(e) and 7(f), as the cloud liquid water path signal is confined almost entirely to the 87 and 164 GHz channels of TEMPEST-D. The sensitivity to liquid clouds with and without three ABI channels is similar, with  $R^2$  values about 0.83. However, given additional cloud sensitive channels from five ABI window and CO<sub>2</sub> bands, liquid cloud retrievals are slightly improved by using TEMPEST+ABI, as the  $R^2$  values increase from about 0.83 to 0.85. Since ice clouds are at a higher altitude and interact with window and CO<sub>2</sub> channels as well as the water-vapor-sounding channels, the 164 to 181 GHz TEMPEST and 6.2 to 13.3  $\mu\text{m}$  ABI channels have different degrees of sensitivity, as shown in Fig. 3(d). Adding ABI channels has larger impacts on the retrieved ice clouds, as the  $R^2$  values increase from 0.782 using only TEMPEST bands to over 0.9 using eight or three combined channels from TEMPEST and ABI. Especially, due to strong sensitivity from ABI channels 8.4 to 13.3  $\mu\text{m}$ , merging five TEMPEST and eight ABI channels gives the best ice cloud retrievals ( $R^2$  value is about 0.93) among three retrieval configurations and significantly constrains retrieved ice water path with less than 50 g/m<sup>2</sup>. Overall, the retrieved liquid and ice clouds are all underestimated compared with the ERA5 profiles. For liquid clouds, this is simply due to the saturation of the cloud water emission signal at roughly 300 to 400 g/m<sup>2</sup> with the available channels. For ice clouds, the primary signal is a brightness temperature depression due to scattering. While this signal does not saturate, thicker ice clouds (> 300 to 400 g/m<sup>2</sup>) are often found in conjunction with liquid clouds in ERA5, leading to brightness temperature signatures that are more difficult to untangle.

#### 4.2. Independent Validation

While the preceding section focused on synthetic brightness temperatures generated from ERA5 profiles, this section uses radiosonde data to validate retrievals from actual observations. The Integrated Global Radiosonde Archive (IGRA) has collected and quality-controlled in situ observations from over 2,800 global stations since 1905, providing vertical profiles of pressure, temperature, humidity, and wind speed and direction. The IGRA dataset can be accessed at <https://www.ncei.noaa.gov/products/weather-balloon/integrated-global-radiosonde-archive>. The IGRA dataset used in the study is version 2.2 and is collocated with TEMPEST-D and GOES-16 ABI observations from 2019 to 2020. To ensure consistency in collocated cases, the observations from these three datasets are all within 1 hour and 1 degree latitude/longitude. Because the OE retrieval discussed here is limited to oceans, the radiosondes used in this study are limited to coastal regions. To avoid surface contaminations, the collocated TEMPEST-D measurements are moved over the ocean to ensure that ~30 km (the sensor FOV) in all directions of the TEMPEST-D pixel is free of land. The displaced footprints must have the same cloud conditions (clear sky or cloudy) as determined by GOES-16 cloud products at the radiosonde location to ensure these locations are under similar atmospheric conditions. There are 19 collocated coastal IGRA stations in the GOES-16 FOV, as shown in Fig. 8. The

Deleted: c) and (

Deleted: e) and (f

Deleted: c) and (

Deleted: c

Deleted: f

Deleted: c

Deleted: d

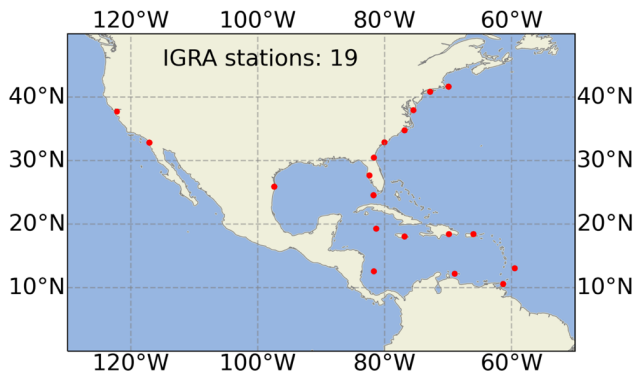
Deleted: 7

Deleted: three

Deleted: -sounding

Deleted: about 0.9 using eight combined channels from TEMPEST and ABI...

576 collocated IGRA sites are around North America and the Caribbean Sea. Given GOES-16 cloud  
577 information, there are 104 collocated cases, of which 10 cases are cloud-free, and 94 cases are under  
578 different degrees of cloudy skies, as shown in Fig. 9. The limited number of coincident samples is due  
579 to infrequent TEMPEST-D overpasses coupled with infrequent (twice daily) radiosonde launches and  
580 frequent data downlink problems of TEMPEST-D, leaving only this limited set of radiosondes to  
581 compare to.  
582  
583



584  
585 Figure 8. Map of collocated IGRA stations. The total number of collocated sites is 19, as marked in the  
586 red circle dots.  
587  
588

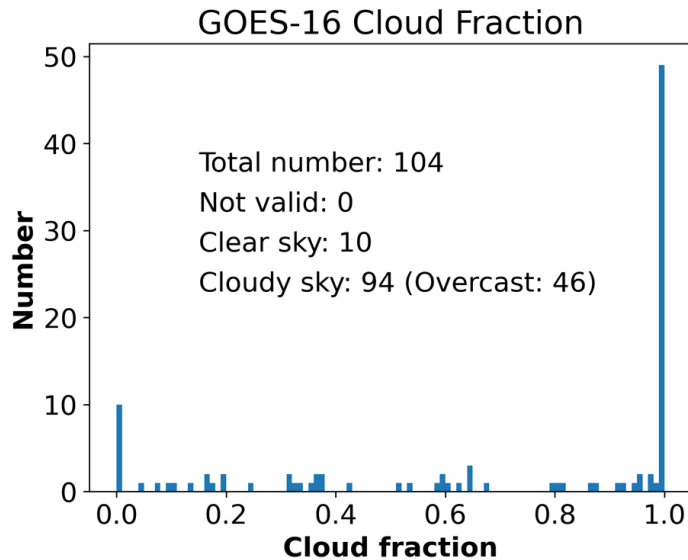


Figure 9. The histogram of GOES-16 derived cloud fraction at the collocated locations. The total number of collocated cases is 104, including 10 clear and 94 cloudy cases.

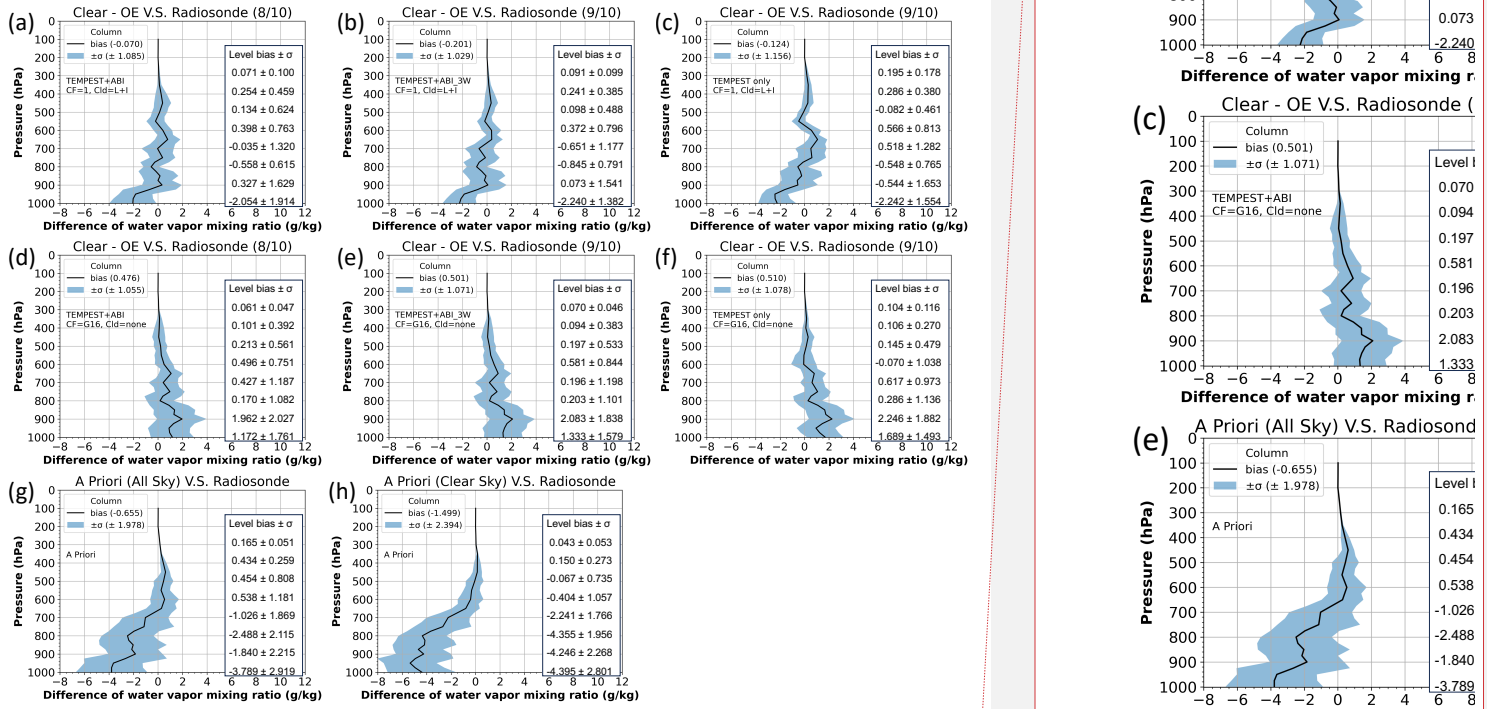
With additional cloud information from GOES-16 products, water vapor retrievals are validated with various levels of cloud information from the geostationary observations, as described in Table 1. The most significant difference is that the algorithm does not retrieve clouds when the area is cloud-free (as determined by ABI's cloud mask) and uses observations from all channels to retrieve water vapor profiles only. Figure 10 shows the error in the retrieved water vapor profiles in clear skies, with biases and standard deviations of column errors listed in Table 2. Only nine cases converged among ten clear sky cases under four different retrieval settings for using only TEMPEST bands and merged TEMPEST and ABI three water vapor channels; using five TEMPEST and eight ABI bands has slightly reduced the retrieval rate, which is eight out of ten cases. Experiments are performed with and without GOES-16 information. If GOES-16 cloud products are not used, the cloud fraction is set to 1.0, implying that clouds covering the FOV are possible, although the retrieval can set the cloud water path to zero. The convergence criteria from Eq. (2) are set to 0.8 for retrievals using TEMPEST-D and ABI three or eight channels and are 0.5 for using TEMPEST-D five bands, as mentioned in section 3 (either 5 or 8 layers of clouds/water vapor in this case).

Table 2. Compared with IGRA radiosonde observations, the column bias and standard deviation of retrieved water vapor mixing ratio under the clear sky conditions. The statistic values are evaluated based on all converged eight clear sky cases for the TEMPEST+ABI sensor configuration and nine clear sky cases for using TEMPEST and TEMPEST+ABI 3W channels. CF means cloud fraction.

Sensors	Using GOES-16 cloud products	
	No set CF to 1	Yes set CF to 0
<u>TEMPEST+ABI (13 channels)</u>	<u>-0.070 ± 1.085 g/kg</u>	<u>0.476 ± 1.055 g/kg</u>
TEMPEST+ABI_3W (8 channels)	-0.201 ± 1.029 g/kg	0.501 ± 1.071 g/kg
TEMPEST (5 channels)	-0.124 ± 1.156 g/kg	0.510 ± 1.078 g/kg

Formatted Table

Formatted Table



617  
618 Figure 10. The water vapor mixing ratio difference between retrievals and radiosonde measurement  
619 (retrievals minus IGRA) in the GOES-16 observed clear skies. Retrievals use thirteen bands from  
620 TEMPEST-D and GOES-16 ABI in Figures (a) and (d), use five TEMPEST-D and three ABI water-vapor-  
621 sounding channels in Figures (b) and (e), and use only TEMPEST-D channels in Figures (c) and (f).  
622 Retrievals in Figures (a) to (c) assume existing liquid and ice clouds with cloud fraction = 1 and use all-  
623 sky a priori, and retrievals in Figures (d) to (f) set no clouds with cloud fraction = 0 and use clear sky a

- Deleted:
- Deleted: c) and
- Deleted: b
- Deleted: d
- Deleted: and (b
- Deleted: c) and (

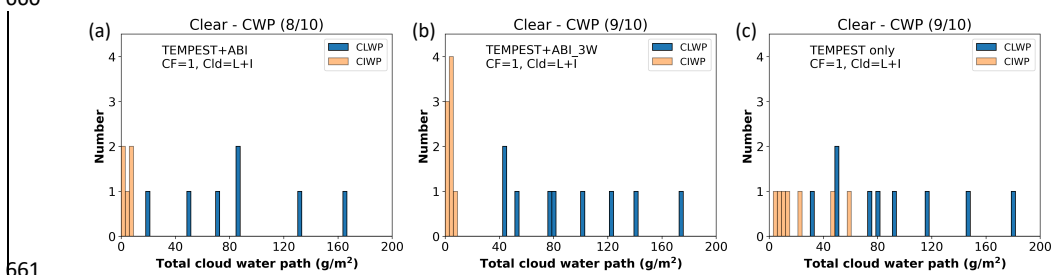
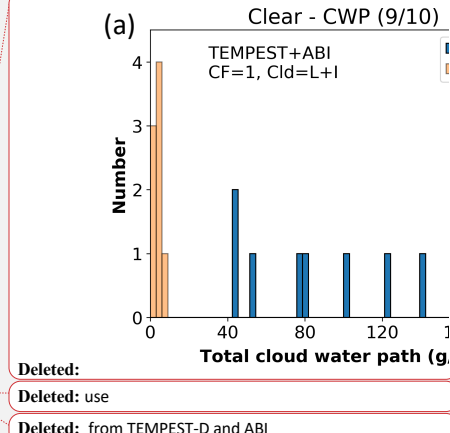
630 priori. In the retrievals, the biases of the water vapor a priori information derived from all-sky  
 631 conditions are shown in Figure (g), and obtained from clear skies are presented in Figure (h). The solid  
 632 black lines are the bias value, and the blue shade regions indicate the standard deviation ( $\sigma$ ). The  
 633 included table quantifies the retrieval performance from 300 to 1000 hPa for every 100 hPa. The  
 634 number in the parentheses indicates the number of all converged cases out of all clear sky cases. G16  
 635 means GOES-16 products, and L+I indicates liquid and ice clouds.

637  
 638 The additional eight (6.2 to 13.3  $\mu\text{m}$ ) as well as three (6.2 to 7.3  $\mu\text{m}$ ) channels from ABI help to  
 639 constrain water vapor profiles, as shown in the reduced column error standard deviations as well as  
 640 the layer biases and standard deviations, although the differences are smaller than they were with the  
 641 simulated results. Compared with TEMPEST-only (Figs. 10(c) and 10(f)), the retrieved water vapor  
 642 profiles above 800 hPa are visibly less biased after including eight (Figs. 10(a) and 10(d)) or three (Figs.  
 643 10(b) and 10(e)) ABI channels. The overall statistics are not as impressive because much of the water  
 644 vapor is in the 1000 to 800 hPa layer, which is not improved by additional three ABI water-vapor-  
 645 sounding channels. However, with extra information from five ABI window and CO<sub>2</sub> bands, water vapor  
 646 retrievals have slightly improvement around the surface, leading to smaller entire retrieval biases and  
 647 standard deviations among these three sensor configurations. Figures 11(a) to 11(c) present the  
 648 erroneous retrieved liquid and ice clouds under the clear conditions corresponding to Figs. 10(a) to  
 649 10(c), respectively. No clouds are estimated in retrievals in Figs. 10(d) to 10(f), as this information is  
 650 taken from the IR channels. Because parts of the water vapor signals are falsely attributed to clouds,  
 651 retrieved water vapor profiles are underestimated when clouds are derived, as in Figs. 10(a) to 10(c)  
 652 and 11. On the other hand, retrieved water vapor profiles are overestimated in Figs. 10(d) to 10(f)  
 653 when the scene is forced to be cloud-free based on ABI information. We speculate that, as with the  
 654 synthetic retrievals, the bias from ERA5 information in Fig. 10(h) under clear sky assumptions is even  
 655 larger than if all sky ERA5 a priori in Fig. 10(g) is used. This leads to even larger biases in the initial  
 656 iteration, which the retrievals can only partially correct without adding small amounts of cloud water  
 657 to the scene. Conversely, it is also possible that the small number of cases (8 or 9) simply are not  
 658 representative.

Deleted: e  
 Deleted: f

Deleted: three  
 Deleted: water-vapor-sounding  
 Deleted: b  
 Deleted: d  
 Deleted: ABI channels  
 Deleted: c).  
 Deleted: ABI channels. Figures 11(a) and 11(b)

Deleted: and  
 Deleted: b  
 Deleted: c) and  
 Deleted: d  
 Deleted: ),  
 Deleted: b),  
 Deleted: c) and  
 Deleted: d  
 Deleted: f  
 Deleted: e



661 Figure 11. Retrieved total cloud water path for liquid and ice clouds in the clear sky cases with no cloud  
 662 information from GOES-16. Retrievals in Figure (a) and (b), in addition to five TEMPEST channels, use  
 663 eight ABI channels and three ABI water vapor bands, respectively, and use only TEMPEST-D channels  
 664

Deleted:  
 Deleted: use  
 Deleted: from TEMPEST-D and ABI



687 for Figure (c). The number in the parentheses indicates the number of all converged cases among all  
688 clear sky cases. L+I indicates liquid and ice clouds.

690  
691 Water vapor retrieval errors under cloudy conditions for various assumptions of cloud knowledge are  
692 presented in Fig. 12, with the corresponding bias and standard deviation of column errors listed in  
693 Table 3. Although cases used in Table 3 and Fig. 12 have all ABI and TEMPEST-D observations and all  
694 cloud information, this is not the case for all other pixels. Therefore, Table 3 and Figure 12 show the  
695 possible results from nine different retrieval configurations using different degrees of cloud status and  
696 using TEMPEST-only or with measurements from eight or three ABI channels. The retrieval  
697 configurations in cloudy cases are listed in Table 1. Due to lack of humidity sensitivity of ABI window  
698 and CO<sub>2</sub> bands below clouds as Fig. 3(d), in comparisons with adding three ABI water-vapor-sounding  
699 channels, using eight ABI bands doesn't improve water vapor retrievals and has much less retrieval  
700 rate. Retrievals in Figs. 12(a) to 12(c) have no information about clouds. In contrast, Figs. 12(d) to 12(j)  
701 show results with different degrees of knowledge about clouds from ABI. Figures 12(d) to 12(f) use only  
702 cloud fractions. In the scenarios of no cloud information from ABI in Figs 12(a) to 12(c), water vapor  
703 retrievals using TEMPEST+ABI and TEMPEST+ABI 3W have improvement above 500 hPa, between 700  
704 and 800 hPa, and around the surface. When only cloud fraction is available from GOES-16 cloud  
705 products, Figs 12(d) to 12(f) show that adding eight or three ABI bands improves overall water vapor  
706 retrievals except for around 900 hPa. If the cloud fraction, cloud height, and cloud phase are all  
707 available from the cloud products as in Figs 12(g) to 12(j), water vapor retrievals using different  
708 degrees of ABI measurements have improvement around 300, 400, and 600 hPa and have minor or no  
709 improvement on the other levels. In general, when retrievals use the same cloud status, column  
710 average water vapor retrieval biases using TEMPEST and ABI observations are smaller than using  
711 TEMPEST-only measurements, as in comparisons among Figs 12(a) to 12(c), Figs 12(d) to 12(f), and Figs  
712 12(g) to 12(j). While column average water vapor retrievals do not improve significantly by adding  
713 cloud fraction information, when cloud fractions are specified, quantitative comparisons show some  
714 improvements between 500 and 700 hPa and around the surface for TEMPEST+ABI retrievals in Figs.  
715 12(a) and 12(d) and for TEMPEST+ABI 3W retrievals in Figs. 12(b) and 12(e), and present some  
716 improvements above 400 hPa and around 600 hPa and the surface for TEMPEST-only retrievals in Figs.  
717 12(c) and 12(f).

718  
719 Additional cloud information in the form of cloud fraction, cloud height, and cloud phase from GOES-16  
720 products are shown in Figs. 12(g) to 12(j). When retrievals use more cloud information from GOES-16  
721 (cloud fraction, height, and phase), water vapor retrieval biases shown in Fig. 12(h) are about half of  
722 the biases in Figs. 12(b) and 12(e) around 600 hPa and shown in Fig. 12(i) are improved above 700 hPa  
723 except for around 600 hPa compared with Figs. 12(c) and 12(f), but retrievals have no or minor  
724 improvements above 700 hPa in Fig. 12(g) compared with Figs. 12(a) and 12(d). Water vapor retrievals  
725 around lower layers in Figs. 12(g) to 12(i) show larger biases and little difference among using only  
726 TEMPEST, TEMPEST+ABI 3W or TEMPEST+ABI. In cloudy conditions, the only channels with sensitivity  
727 to the low-level water vapor are the TEMPEST 87 and 164 GHz channels, as shown in Fig. 3(d).  
728 However, some overfitting appears to be taking place between 700 and 1000 hPa. The authors  
729 speculate that the ice scattering properties assumed in the retrieval's forward model may cause excess  
730 depression at 87 and 164GHz channels, which in turn, requires the algorithm to increase the cloud

Deleted: b

Deleted: Figure

Deleted: six

Deleted: ABI

Deleted: .

Deleted: and

Deleted: b

Deleted: c

Deleted: f

Deleted: c) and

Deleted: d

Deleted: and

Deleted: b

Deleted: c) and

Deleted: d

Deleted: e) and

Deleted: f

Deleted: with

Deleted: and

Deleted: b

Deleted: c) and 12(

Deleted: e) and

Deleted: f

Deleted: c

Moved (insertion) [1]

Moved (insertion) [2]

Moved (insertion) [3]

Deleted: 12(b) and 12(d).

water and water vapor to match the brightness temperatures in those channels. Meanwhile, since MW and IR have different sensitivity to the clouds, the cloud properties obtained from ABI cloud products are derived from VIS/IR bands (Goodman et al., 2019) may not be representative to more cloud transparent MW channels, adding more uncertainties in retrievals.

The water vapor retrieval errors are further decomposed by cloud fraction from GOES-16, shown in Fig. 13, using various retrieval configurations shown in Table 1 under cloudy conditions. Since not enough retrievals are obtained by TEMPEST+ABI configurations, Figure 13 only presents errors from retrievals using TEMPEST+ABI 3W and TEMPEST-only sensors. Among six retrieval settings, the estimated water vapor profiles are nearly unbiased when the cloud fraction is between 0.4 and 0.6 with about 0.5 g/kg of error standard deviation, as these amounts of clouds provide enough signals and do not entirely obscure signals underneath. For low cloud fractions, assigning the cloud fraction from GOES-16 ABI leads to a bias, although the standard deviation is roughly the same as if a cloud fraction of 1 is assigned. This can be attributed to the nonlinear response of the MW radiances at 87 and 164 GHz to cloud water content. When the assigned cloud fraction is small, the retrieval must assign all the necessary cloud liquid water to a small cloud fraction, saturating the radiance signals and generally causing poorer retrievals. As was seen in the synthetic retrievals, saturation will cause the cloud water to be underestimated, which will in turn lead to an overestimation in water vapor as the OE tries to balance all radiance terms. If the scene is truly overcast (observed cloud fraction near 1.0), there can be no difference between assigning a cloud fraction of 1.0 as the default assumption or 1.0 as an observed parameter, and this is reflected in the results as well.

Table 3. Column bias and standard deviation of retrieved water vapor mixing ratio in the cloudy skies when compared to IGRA radiosonde observations. Statistics are evaluated based on all covered 51 cloudy sky cases for TEMPEST+ABI sensor configurations and 77 cloudy sky cases for using TEMPEST and TEMPEST+ABI 3W channels.

Sensors	Using GOES-16 cloud products		
	No set CF to 1	Yes set CF from GOES-16	Yes set CF, CH, and CP from GOES-16
TEMPEST+ABI (13 channels)	0.034 ± 1.524 g/kg	0.071 ± 1.509 g/kg	0.488 ± 1.816 g/kg
TEMPEST+ABI 3W (8 channels)	0.007 ± 1.440 g/kg	0.061 ± 1.462 g/kg	0.514 ± 1.665 g/kg
TEMPEST (5 channels)	0.039 ± 1.488 g/kg	0.083 ± 1.488 g/kg	0.575 ± 1.632 g/kg

Moved up [1]: Additional cloud information in the form of cloud fraction, cloud height, and cloud phase from GOES-16 products are shown in Figs.

Moved up [2]: ). When retrievals use more cloud information from GOES-16 (cloud fraction, height, and phase), water vapor retrieval biases shown in Fig.

Moved up [3]: In cloudy conditions, the only channels with sensitivity to the low-level water vapor are the TEMPEST 87 and 164 GHz channels, as shown in Fig. 3(d). However, some overfitting appears to be taking place

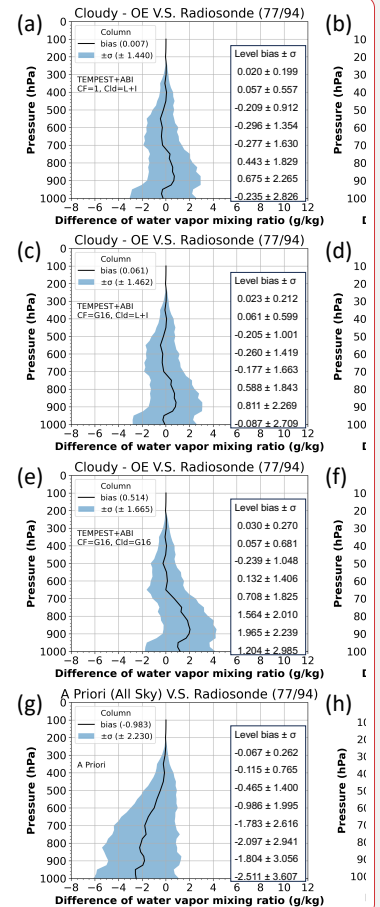
Deleted: 12(e) and 12(f)

Deleted: 12(e) are about half of the biases in Figs. 12(a) and 12(c) around 600 hPa and shown in Fig. 12(f) are significantly improved above 700 hPa except for around 600 hPa compared with 12(b) and 12(d), but lower layers in Fig. 12(e) and 12(f) show larger biases and little difference between using only TEMPEST or TEMPEST+ABI.

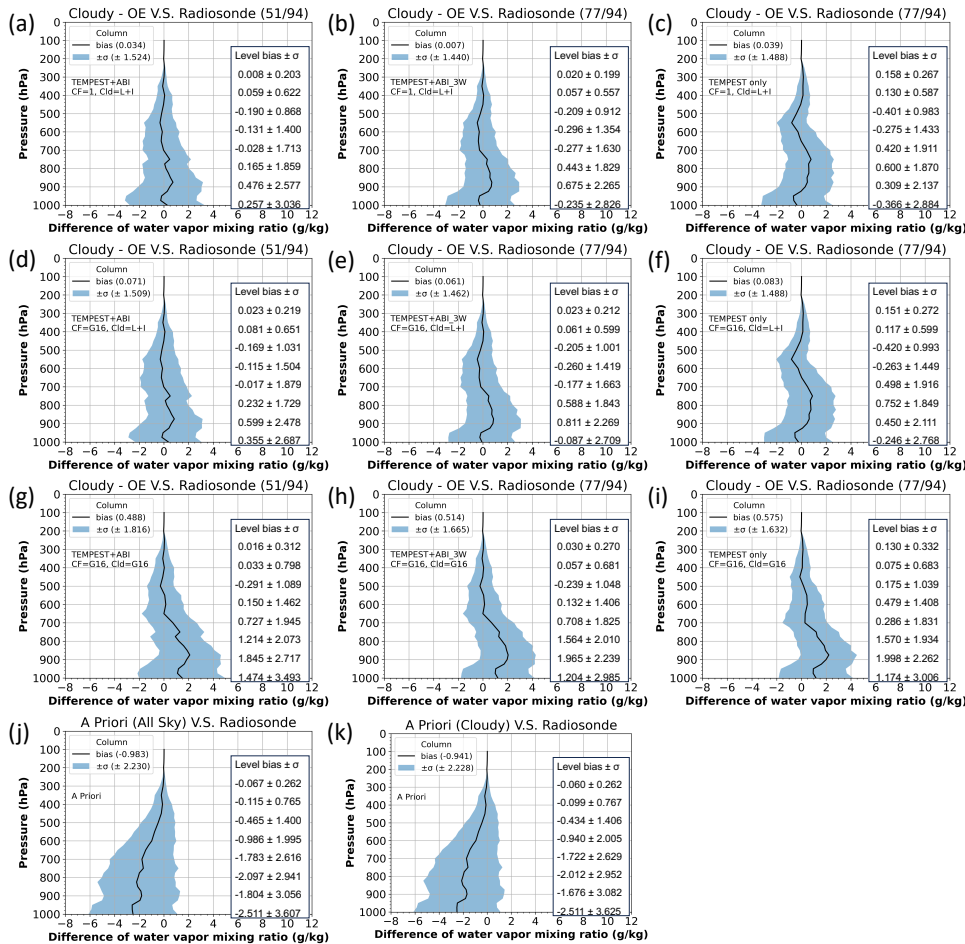
Deleted: . The authors speculate that the ice scattering properties assumed in the retrieval's forward model may cause excess depression at 87 and 164GHz channels, which in turn, requires the algorithm to increase the cloud water and water vapor to match the brightness temperatures in those channels.

Formatted Table

Formatted Table



Deleted:



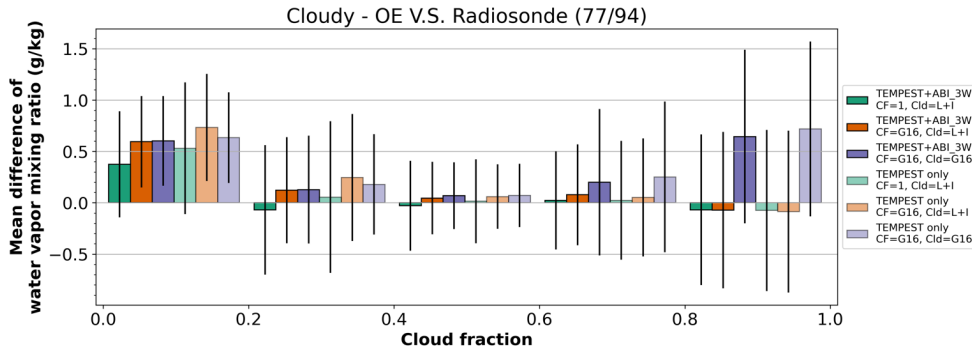
- Deleted: bands from
- Deleted: -D and GOES-16
- Deleted: c),
- Deleted: e
- Deleted: use only TEMPEST-D
- Deleted: d
- Deleted: d
- Deleted: and (b
- Deleted: c) and (
- Deleted: e) and (f
- Deleted: and (b
- Deleted: c
- Deleted: f
- Deleted: g),
- Deleted: h

810

811 Figure 12. The water vapor mixing ratio difference between retrievals and radiosonde measurement  
 812 (retrievals minus IGRA) with GOES-16 observed cloudy conditions. Retrievals use five TEMPEST  
 813 channels with eight ABI bands in Figures (a), (d) and (g) and with three ABI water vapor channels in  
 814 Figures (b), (e) and (h), and use only TEMPEST channels in Figures (c), (f) and (i). Figures (a) to (f) show  
 815 retrievals assuming liquid and ice clouds with cloud fraction = 1 for Figures (a) to (c) and with cloud  
 816 fraction from GOES-16 cloud mask for Figures (d) to (f). Retrievals in Figures (g) to (i) use cloud fraction,  
 817 height, and phase from GOES-16 products to define cloud layers. Figures (a) to (c) use all-sky a priori,  
 818 and Figures (d) to (i) use cloudy sky a priori. In the retrievals, the biases of the water vapor a priori  
 819 information derived from all-sky conditions are shown in Figure (j) and obtained from cloudy skies are  
 820 presented in Figure (k). The solid black lines are the bias value, and the blue shade regions indicate the

836 standard deviation ( $\sigma$ ). The included table quantifies the retrieval performance from 300 to 1000 hPa  
 837 for every 100 hPa. The number in the parentheses means the number of all converged cases out of all  
 838 cloudy sky cases. G16 means GOES-16 products, and L+I indicates liquid and ice clouds.  
 839

840



841

842 Figure 13. The mean difference between retrieved and radiosonde-observed water vapor profiles  
 843 (retrievals minus IGRA) within different GOES-16 cloud fraction intervals. Assuming both liquid and ice  
 844 clouds exist, the green bars indicate that retrievals use cloud fraction = 1, and the orange bars mean  
 845 that retrievals use only cloud fraction from GOES-16 products. The purple bars show retrievals using  
 846 cloud fraction, height, and phase from GOES-16 products. Lighter colors mean retrievals only use  
 847 TEMPEST-D, and darker colors show retrievals using both TEMPEST-D and GOES-16 ABI [three water](#)  
 848 [vapor channels](#). Solid black lines are the range of  $\pm$  standard deviation. The number in the parentheses  
 849 means the number of all converged cases among all cloudy sky cases. G16 means GOES-16 products,  
 850 and L+I indicates liquid and ice clouds.

851

852

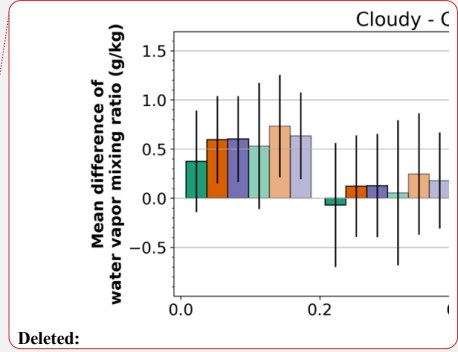
## 853 5. Conclusions

854

855 TEMPEST-D successfully demonstrated the capability of CubeSats radiometers to maintain well-  
 856 calibrated MW signals in five channels from 87 to 181 GHz over a period of almost 3 years. Although  
 857 TEMPEST-D and the TEMPEST instrument currently flying with COWVR on the International Space  
 858 Station are economical and functional, these small MW radiometers fly without an accompanying  
 859 hyperspectral IR sensor typical on operational platforms. GOES-R ABI sensors provide observations of  
 860 the Earth every 1 to 10 minutes depending on the modes, and measure 16 spectral bands from VIS to  
 861 IR with 0.5 to 2.0 km ground resolution. Given such unique ABI observations with high spatial and  
 862 temporal resolution, supplemental information from ABI enhances the ability of TEMPEST as well as  
 863 other similar CubeSats to infer the states of the atmosphere.

864

865 Along with five TEMPEST MW bands, this study presented improvements in humidity profiles that are  
 866 possible when TEMPEST retrievals are supplemented with three IR water-vapor-sounding channels [and](#)  
 867 [five IR window and CO<sub>2</sub> bands](#) available from GOES ABI. A number of positive outcomes were shown in



Deleted:

Deleted: sensors.

870 this paper. In the sensitivity tests comparing the combined MW/IR retrievals to MW-only capabilities,  
871 the effective vertical resolution increases, as seen by smaller layer errors, under both clear and cloudy  
872 conditions. The retrieved water vapor profiles were validated using independent IGRA humidity-  
873 sounding data from 2019 to 2020. During these two years of routine TEMPEST-D operations, only 104  
874 IGRA cases (10 cases are clear scenes, 94 under different cloudy conditions) exist. Consistent with the  
875 sensitivity tests, the validation also showed the advantages of using GOES-16 cloud products and  
876 additional ABI IR channels in water vapor sounding under different sky conditions.

Deleted: three

878 In clear sky regions, with ABI's ability to unambiguously characterize these scenes as cloud-free,  
879 retrievals are improved merely by forcing the scene to be cloud-free, and by gaining more information  
880 around the lower part of the atmosphere from ABI window and CO<sub>2</sub> bands. While statistics in Figs. 10  
881 and 11 indicate that column average biases grow slightly when the ABI cloud mask is used to identify  
882 the scene as cloud-free, the profiles themselves show clear improvement above the boundary layer.  
883 Near the surface, retrievals are sensitive to the large biases in the prior data in these comparisons, and  
884 it is difficult to draw conclusions. Nonetheless, adding three ABI channels slightly decreased overall  
885 biases from 0.510 to 0.501 g/kg and biases are further reduced to 0.476 g/kg using extra five ABI  
886 window and CO<sub>2</sub> channels with about the same error standard deviation of 1 g/kg.

Deleted: .

887 Under cloudy conditions, water vapor retrievals have different degree of improvements when adding  
888 ABI, as shown in Figs. 12 and 13, and results are generally improved when cloud fraction information is  
889 added to the retrieval, except for very small cloud fractions where saturation in the cloudy portion of  
890 the footprint becomes an issue. Adding cloud top and cloud phase information causes errors larger  
891 than 0.5 g/kg. This is likely due to incorrect assumptions about the ice cloud scattering properties.

Deleted: are significantly improved

893 This study explored the advantages of merging TEMPEST-D, with ABI observations from GOES-16 to  
894 improve water vapor soundings. However, ABI-like sensors, whether on the Himawari series satellites  
895 (Bessho et al., 2016) or other platforms, cover the entire globe, providing multi-spectral, high spatial,  
896 and high temporal observations. While we can only speculate, we assume that hyperspectral IR (Li et  
897 al., 2022) planned for the next generation of geostationary satellites will significantly improve the  
898 sounding capabilities in clear sky regions. This should lead to better overall retrievals in cloudy skies as  
899 well, if one can extrapolate results from Figs. 6 and 7, which show the improvements to the passive  
900 MW retrievals when more information is added to the retrievals. With more and more CubeSats being  
901 launched, including COWVR and TEMPEST on Space Test Program-Houston 8  
902 (<https://podaac.jpl.nasa.gov/COWVR-TEMPEST>), TROPICS (Blackwell et al., 2018;  
903 <https://tropics.ll.mit.edu/CMS/tropics>), and the INvestigation of Convective UpdraftS (INCUS; van den  
904 Heever et al., 2022; <https://incus.colostate.edu>) missions, these missions will all benefit from more  
905 sounding and cloud information from ABI-like sensors or even from geostationary hyperspectral IR  
906 sensors, enhancing the capability of CubeSats.

#### 908 Code availability

909 CRTM is available through the website <https://github.com/JCSDA/crtm>, and MonoRTM can be assessed  
910 by the website <https://github.com/AER-RC/monoRTM>.

913

917 **Data availability**

918

919 The TEMPEST-D datasets can be downloaded through the website <https://tempest.colostate.edu> after  
920 registration. The GOES-16 products are archived at CLASS (<https://www.avi.class.noaa.gov>). The IGR  
921 dataset is available at [https://www.ncei.noaa.gov/products/weather-balloon/integrated-global-](https://www.ncei.noaa.gov/products/weather-balloon/integrated-global-radiosonde-archive)  
922 [radiosonde-archive](https://www.ncei.noaa.gov/products/weather-balloon/integrated-global-radiosonde-archive). The ERA5 dataset can be accessed by the website  
923 <https://www.ecmwf.int/en/forecasts/dataset/ecmwf-reanalysis-v5>.

924

925 **Author contribution**

926

927 CPK and CK designed and improved the experiments. CPK is responsible for collecting and processing  
928 data. CPK prepared the manuscript. CPK and CK discussed the results and revised the manuscript.

929

930 **Competing interests**

931

932 The contact author has declared that none of the authors has any competing interests.

933

934 **Acknowledgments**

935

936 This study was supported by NASA grant 80NM0078F0617 as part of an effort to improve water vapor  
937 soundings from the TEMPEST CubeSat radiometer on Space Test Program-Houston 8. The authors  
938 appreciate the reviewers' thorough comments, which greatly improved the paper.

939

940 **References**

941

942 Aires, F.: Measure and exploitation of multisensor and multiwavelength synergy for remote sensing: 1.  
943 Theoretical considerations, *J. Geophys. Res.*, 116, D02301–D02301,  
944 <https://doi.org/10.1029/2010JD014701>, 2011.

945

946 Aires, F., Paul, M., Prigent, C., Rommen, B., and Bouvet, M.: Measure and exploitation of multisensor  
947 and multiwavelength synergy for remote sensing: 2. Application to the retrieval of atmospheric  
948 temperature and water vapor from MetOp, *J. Geophys. Res.*, 116, D02302–D02302,  
949 <https://doi.org/10.1029/2010JD014702>, 2011.

950

951 Aires, F., Aznay, O., Prigent, C., Paul, M., and Bernardo, F.: Synergistic multi-wavelength remote sensing  
952 versus a posteriori combination of retrieved products: Application for the retrieval of atmospheric  
953 profiles using MetOp-A, *J. Geophys. Res.*, 117, D18304, <https://doi.org/10.1029/2011JD017188>, 2012.

954

955 Berg, W., Brown, S. T., Lim, B. H., Reising, S. C., Goncharenko, Y., Kummerow, C. D., Gaier, T. C., and  
956 Padmanabhan, S.: Calibration and validation of the TEMPEST-D CubeSat radiometer, *IEEE Trans.*  
957 *Geosci. Remote Sens.*, 59, 4904–4914, <https://doi.org/10.1109/TGRS.2020.3018999>, 2021.

958

959 Bessho, K., Date, K., Hayashi, M., Ikeda, A., Imai, T., Inoue, H., Kumagai, Y., Miyakawa, T., Murata, H.,  
960 Ohno, T., Okuyama, A., Oyama, R., Sasaki, Y., Shimazu, Y., Shimoji, K., Sumida, Y., Suzuki, M., Taniguchi,  
961 H., Tsuchiyama, H., Uesawa, D., Yokota, H., and Yoshida, R.: An introduction to Himawari-8/9 - Japan's  
962 new-generation geostationary meteorological satellites, *J. Meteorolog. Soc. Jpn.*, 94, 151–183,  
963 <https://doi.org/10.2151/jmsj.2016-009>, 2016.

964

965 Blackwell, W. J., Braun, S., Bennartz, R., Velden, C., DeMaria, M., Atlas, R., Dunion, J., Marks, F., Rogers,  
966 R., Annane, B., and Leslie, R. V.: An overview of the TROPICS NASA Earth Venture Mission, *Q. J. R.*  
967 *Meteorolog. Soc.*, 144, 16–26, <https://doi.org/10.1002/qj.3290>, 2018.

968

969 Bohren, C. F. and Huffman, D. R.: *Absorption and Scattering of Light by Small Particles*, Wiley, New  
970 York, 530 pp., <https://doi.org/10.1002/9783527618156>, 1998.

971

972 Boukabara, S.-A., Garrett, K., Chen, W., Iturbide-Sanchez, F., Grassotti, C., Kongoli, C., Chen, R., Liu, Q.,  
973 Yan, B., Weng, F., Ferraro, R., Kleespies, T. J., and Meng, H.: MiRS: An all-weather 1DVAR satellite data  
974 assimilation and retrieval system, *IEEE Trans. Geosci. Remote Sens.*, 49, 3249–3272,  
975 <https://doi.org/10.1109/TGRS.2011.2158438>, 2011.

976

977 Boukabara, S.-A., Garrett, K., Grassotti, C., Iturbide-Sanchez, F., Chen, W., Jiang, Z., Clough, S. A., Zhan,  
978 X., Liang, P., Liu, Q., Islam, T., Zubko, V., and Mims, A.: A physical approach for a simultaneous retrieval  
979 of sounding, surface, hydrometeor, and cryospheric parameters from SNPP/ATMS, *J. Geophys. Res.:*  
980 *Atmos.*, 118, 12,600–12,619, <https://doi.org/10.1002/2013JD020448>, 2013.

981



982 Boukabara, S.-A., Garrett, K., and Grassotti, C.: Dynamic inversion of global surface microwave  
983 emissivity using a 1DVAR approach, *Remote Sens.*, 10, 679–679, <https://doi.org/10.3390/rs10050679>,  
984 2018.

985

986 Brown, S. T., Tanner, A., Reising, S. C., and Berg, W.: Single-point calibration for microwave sounders:  
987 Application to TEMPEST-D, *J. Atmos. Oceanic Technol.*, <https://doi.org/10.1175/JTECH-D-22-0063.1>,  
988 2023.

989

990 Clough, S. A., Shephard, M. W., Mlawer, E. J., Delamere, J. S., Iacono, M. J., Cady-Pereira, K.,  
991 Boukabara, S., and Brown, P. D.: Atmospheric radiative transfer modeling: A summary of the AER  
992 codes, *J. Quant. Spectrosc. Radiat. Transfer*, 91, 233–244, <https://doi.org/10.1016/j.jqsrt.2004.05.058>,  
993 2005.

994

995 Draine, B. T. and Flatau, P. J.: Discrete-dipole approximation for scattering calculations, *J. Opt. Soc. Am.*  
996 *A*, 11, 1491, <https://doi.org/10.1364/JOSAA.11.001491>, 1994.

997

998 Duncan, D. I. and Kummerow, C. D.: A 1DVAR retrieval applied to GMI: Algorithm description,  
999 validation, and sensitivities, *J. Geophys. Res.: Atmos.*, 121, 7415–7429,  
1000 <https://doi.org/10.1002/2016JD024808>, 2016.

1001

1002 Elsaesser, G. S. and Kummerow, C. D.: Toward a fully parametric retrieval of the nonraining parameters  
1003 over the global oceans, *J. Appl. Meteorol. Climatol.*, 47, 1599–1618,  
1004 <https://doi.org/10.1175/2007JAMC1712.1>, 2008.

1005

1006 Field, P. R., Heymsfield, A. J., and Bansemer, A.: Snow size distribution parameterization for midlatitude  
1007 and tropical ice clouds, *J. Atmos. Sci.*, 64, 4346–4365, <https://doi.org/10.1175/2007JAS2344.1>, 2007.

1008

1009 Gambacorta, A., Barnet, C., Wolf, W., Goldberg, M., King, T., Ziong, X., Nalli, N., Maddy, E., and  
1010 Divakarla, M.: The NOAA Unique CrIS/ATMS Processing System (NUCAPS): First light retrieval results,  
1011 in: In Proceedings of the ITWG meeting, ITWG, Toulouse, France, 2012.

1012

1013 GOES-R Series: Mission Requirements Document (MRD) July 28, 2022, 2022.

1014

1015 Goodman, S. J., Schmit, T. J., Daniels, J., and Redmon, R. J. (Eds.): The GOES-R Series: A New Generation  
1016 of Geostationary Environmental Satellites, Elsevier, <https://doi.org/10.1016/C2015-0-06249-9>, 2019.

1017

1018 Hersbach, H., Bell, B., Berrisford, P., Hirahara, S., Horányi, A., Muñoz-Sabater, J., Nicolas, J., Peubey, C.,  
1019 Radu, R., Schepers, D., Simmons, A., Soci, C., Abdalla, S., Abellan, X., Balsamo, G., Bechtold, P., Biavati,  
1020 G., Bidlot, J., Bonavita, M., Chiara, G., Dahlgren, P., Dee, D., Diamantakis, M., Dragani, R., Flemming, J.,  
1021 Forbes, R., Fuentes, M., Geer, A., Haimberger, L., Healy, S., Hogan, R. J., Hólm, E., Janisková, M., Keeley,  
1022 S., Laloyaux, P., Lopez, P., Lupu, C., Radnoti, G., Rosnay, P., Rozum, I., Vamborg, F., Villaume, S., and  
1023 Thépaut, J.: The ERA5 global reanalysis, *Q. J. R. Meteorolog. Soc.*, 146, 1999–2049,  
1024 <https://doi.org/10.1002/qj.3803>, 2020.

1025

1026 Johnson, B. T., Dang, C., Stegmann, P., Liu, Q., Moradi, I., and Auligne, T.: The Community Radiative  
1027 Transfer Model (CRTM): Community-focused collaborative model development accelerating research  
1028 to operations, *Bull. Am. Meteorol. Soc.*, <https://doi.org/10.1175/BAMS-D-22-0015.1>, 2023.  
1029  
1030 Kazumori, M. and English, S. J.: Use of the ocean surface wind direction signal in microwave radiance  
1031 assimilation, *Q. J. R. Meteorolog. Soc.*, 141, 1354–1375, <https://doi.org/10.1002/qj.2445>, 2015.  
1032  
1033 Kulie, M. S., Bennartz, R., Greenwald, T. J., Chen, Y., and Weng, F.: Uncertainties in microwave  
1034 properties of frozen precipitation: Implications for remote sensing and data assimilation, *J. Atmos. Sci.*,  
1035 67, 3471–3487, <https://doi.org/10.1175/2010JAS3520.1>, 2010.  
1036  
1037 Li, J., Schmit, T. J., Jin, X., Martin, G., and Li, Z.: GOES-R Advanced Baseline Imager (ABI) Algorithm  
1038 Theoretical Basis Document for Legacy Atmospheric Moisture Profile, Legacy Atmospheric  
1039 Temperature Profile, Total Precipitable Water, and Derived Atmospheric Stability Indices, Version 3.1,  
1040 2019.  
1041  
1042 Li, J., Menzel, W. P., Schmit, T. J., and Schmetz, J.: Applications of geostationary hyperspectral infrared  
1043 sounder observations: Progress, challenges, and future perspectives, *Bull. Am. Meteorol. Soc.*, 103,  
1044 E2733–E2755, <https://doi.org/10.1175/BAMS-D-21-0328.1>, 2022.  
1045  
1046 Liu, G.: A database of microwave single-scattering properties for nonspherical ice particles, *Bull. Am.*  
1047 *Meteorol. Soc.*, 89, 1563–1570, <https://doi.org/10.1175/2008BAMS2486.1>, 2008.  
1048  
1049 Liu, Q., van Delst, P., Chen, Y., Groff, D., Han, Y., Collard, A., Weng, F., Boukabara, S.-A., and Derber, J.:  
1050 Community Radiative Transfer Model for radiance assimilation and applications, in: IGARSS 2012 - 2012  
1051 IEEE International Geoscience and Remote Sensing Symposium, Munich, Germany, 3700–3703,  
1052 <https://doi.org/10.1109/IGARSS.2012.6350612>, 2012.  
1053  
1054 Ma, Z., Li, Z., Li, J., Schmit, T. J., Cucurull, L., Atlas, R., and Sun, B.: Enhance low level temperature and  
1055 moisture profiles through combining NUCAPS, ABI observations, and RTMA analysis, *Earth Space Sci.*, 8,  
1056 <https://doi.org/10.1029/2020EA001402>, 2021.  
1057  
1058 Milstein, A. B. and Blackwell, W. J.: Neural network temperature and moisture retrieval algorithm  
1059 validation for AIRS/AMSU and CrIS/ATMS, *J. Geophys. Res.: Atmos.*, 121, 1414–1430,  
1060 <https://doi.org/10.1002/2015JD024008>, 2016.  
1061  
1062 Nowell, H., Liu, G., and Honeyager, R.: Modeling the microwave single-scattering properties of  
1063 aggregate snowflakes, *J. Geophys. Res.: Atmos.*, 118, 7873–7885, <https://doi.org/10.1002/jgrd.50620>,  
1064 2013.  
1065  
1066 Padmanabhan, S., Gaier, T. C., Tanner, A. B., Brown, S. T., Lim, B. H., Reising, S. C., Stachnik, R., Bendig,  
1067 R., and Cofield, R.: TEMPEST-D radiometer: Instrument description and prelaunch calibration, *IEEE*  
1068 *Trans. Geosci. Remote Sens.*, 59, 10213–10226, <https://doi.org/10.1109/TGRS.2020.3041455>, 2021.  
1069

1070 Radhakrishnan, C., Chandrasekar, V., Reising, S. C., and Berg, W.: Rainfall estimation from TEMPEST-D  
1071 CubeSat observations: A machine-learning approach, *IEEE J. Sel. Top. Appl. Earth Obs. Remote Sens.*,  
1072 15, 3626–3636, <https://doi.org/10.1109/JSTARS.2022.3170835>, 2022.  
1073  
1074 Reising, S. C., Gaier, T. C., Padmanabhan, S., Lim, B. H., Heneghan, C., Kummerow, C. D., Berg, W.,  
1075 Chandrasekar, V., Radhakrishnan, C., Brown, S. T., Carvo, J., and Pallas, M.: An earth venture in-space  
1076 Technology Demonstration Mission for Temporal Experiment for Storms and Tropical Systems  
1077 (TEMPEST), in: *IGARSS 2018 - 2018 IEEE International Geoscience and Remote Sensing Symposium*,  
1078 Valencia, 6301–6303, <https://doi.org/10.1109/IGARSS.2018.8517330>, 2018.  
1079  
1080 Ringerud, S., Kulie, M. S., Randel, D. L., Skofronick-Jackson, G. M., and Kummerow, C. D.: Effects of ice  
1081 particle representation on passive microwave precipitation retrieval in a Bayesian scheme, *IEEE Trans.*  
1082 *Geosci. Remote Sens.*, 57, 3619–3632, <https://doi.org/10.1109/TGRS.2018.2886063>, 2019.  
1083  
1084 Rodgers, C. D.: *Inverse Methods for Atmospheric Sounding: Theory and Practice*, World Scientific,  
1085 Singapore; River Edge, NJ, 238 pp., 2000.  
1086  
1087 Schmit, T. J., Li, J., Gurka, J. J., Goldberg, M. D., Schrab, K. J., Li, J., and Feltz, W. F.: The GOES-R  
1088 Advanced Baseline Imager and the continuation of current sounder products, *J. Appl. Meteorol.*  
1089 *Climatol.*, 47, 2696–2711, <https://doi.org/10.1175/2008JAMC1858.1>, 2008.  
1090  
1091 Schulte, R. M. and Kummerow, C. D.: An optimal estimation retrieval algorithm for microwave humidity  
1092 sounding channels with minimal scan position bias, *J. Atmos. Oceanic Technol.*, 36, 409–425,  
1093 <https://doi.org/10.1175/JTECH-D-18-0133.1>, 2019.  
1094  
1095 Schulte, R. M., Kummerow, C. D., Berg, W., Reising, S. C., Brown, S. T., Gaier, T. C., Lim, B. H., and  
1096 Padmanabhan, S.: A passive microwave retrieval algorithm with minimal view-angle bias: Application  
1097 to the TEMPEST-D CubeSat mission, *J. Atmos. Oceanic Technol.*, 37, 197–210,  
1098 <https://doi.org/10.1175/JTECH-D-19-0163.1>, 2020.  
1099  
1100 Siddans, R., Gerber, D., and Miles, G.: *Optimal Estimation Method retrievals with IASI, AMSU and MHS*  
1101 *measurements: Final Report*, 2015.  
1102  
1103 Siddans, R.: *Water Vapour Climate Change Initiative (WV\_cci) – Phase One, Deliverable 2.2; Version*  
1104 *1.0*, 2019.  
1105  
1106 Sun, B., Reale, A., Tilley, F. H., Pettet, M. E., Nalli, N. R., and Barnett, C. D.: Assessment of NUCAPS S-NPP  
1107 CrIS/ATMS sounding products using reference and conventional radiosonde observations, *IEEE J. Sel.*  
1108 *Top. Appl. Earth Obs. Remote Sens.*, 10, 2499–2509, <https://doi.org/10.1109/JSTARS.2017.2670504>,  
1109 2017.  
1110  
1111 Trent, T., Siddans, R., Kerridge, B., Schröder, M., Scott, N. A., and Remedios, J.: Evaluation of  
1112 tropospheric water vapour and temperature profiles retrieved from MetOp-A by the Infrared and

1113 Microwave Sounding scheme, *Atmos. Meas. Tech.*, 16, 1503–1526, [https://doi.org/10.5194/amt-16-](https://doi.org/10.5194/amt-16-1503-2023)  
1114 [1503-2023](https://doi.org/10.5194/amt-16-1503-2023), 2023.  
1115  
1116 van de Hulst, H. C.: *Light Scattering by Small Particles*, Wiley, New York, 470 pp., 1957.  
1117  
1118 van den Heever, S., Haddad, Z., Tanelli, S., Stephens, G., Posselt, D., Kim, Y., Brown, S., Braun, S., Grant,  
1119 L., Kollias, P., Luo, Z. J., Mace, G., Marinescu, P., Padmanabhan, S., Partain, P., Petersent, W., Prasanth,  
1120 S., Rasmussen, K., Reising, S., Schumacher, C., and the INCUS Mission team: The INCUS Mission, in: EGU  
1121 General Assembly 2022, EGU22-9021, [https://doi.org/doi.org/10.5194/egusphere-egu22-9021](https://doi.org/10.5194/egusphere-egu22-9021), 2022.  
1122  
1123 [Yang, P., Hioki, S., Saito, M., Kuo, C.-P., Baum, B., and Liou, K.-N.: A Review of Ice Cloud Optical](https://doi.org/10.3390/atmos9120499)  
1124 [Property Models for Passive Satellite Remote Sensing, \*Atmosphere\*, 9, 499–499,](https://doi.org/10.3390/atmos9120499)  
1125 <https://doi.org/10.3390/atmos9120499>, 2018.  
1126  
1127 [Yi, B., Ding, S., and Bi, L.: Impacts of cloud scattering properties on FY-3D HIRAS simulations, \*J. Quant.\*](https://doi.org/10.1016/j.jqsrt.2020.106902)  
1128 [Spectrosc. Radiat. Transfer, 246, 106902, https://doi.org/10.1016/j.jqsrt.2020.106902](https://doi.org/10.1016/j.jqsrt.2020.106902), 2020.  
1129